

THE UNIVERSITY OF TULSA

THE GRADUATE SCHOOL

FULLY COUPLED SIMULATION OF GEOMECHANICS AND MULTIPHASE
FLOW IN NATURALLY AND HYDRAULICALLY FRACTURED RESERVOIRS

by
Guotong Ren

A thesis submitted in partial fulfillment of
the requirements for the degree of Master of Science
in the Discipline of Petroleum Engineering

The Graduate School
The University of Tulsa

2016

THE UNIVERSITY OF TULSA
THE GRADUATE SCHOOL

FULLY COUPLED SIMULATION OF GEOMECHANICS AND MULTIPHASE
FLOW IN NATURALLY AND HYDRAULICALLY FRACTURED RESERVOIRS

by
Guotong Ren

A THESIS

APPROVED FOR THE DISCIPLINE OF
PETROLEUM ENGINEERING

By Thesis Committee

_____, Chair
Rami M Younis

Albert C. Reynolds

Michael Keller

COPYRIGHT STATEMENT

Copyright © 2016 by Guotong Ren

All rights reserved. No part of this publication may be reproduced, stored in a retrieval system, or transmitted, in any form or by any means (electronic, mechanical, photocopying, recording, or otherwise) without the prior written permission of the author.

ABSTRACT

Guotong Ren (Master of Science in Petroleum Engineering)

Fully coupled simulation of geomechanics and multiphase flow in naturally and hydraulically fractured reservoirs

Directed by Rami Younis

72, pp., Chapter 5: Conclusions

(291 words)

Unconventional reservoirs are typically comprised of a multicontinuum stimulated formation with complex fracture networks that have a wide range of length scales and geometries. While hydraulic fractures may be propped with a varying concentration field of proppant, natural fractures are predominantly supported by pore pressure. A timely topic in the simulation of unconventional petroleum resources is in coupling the geomechanics of the fractured media to the multiphase fluid flow and transport. This coupling is essential for a basic understanding of a number of important practical questions.

To adequately capture the effects of the multiscaled fracture system in terms of both flow and geomechanics, we develop a mixed approach that fully couples an extended finite element method (XFEM) to a hybrid multiphase flow model that couples an embedded-discrete-fracture model (EDFM) with multiple interacting continua (MINC).

This optimized model can reduce the computational cost that is associated with the widely applied unstructured mesh approaches. A Cartesian mesh is used and the two numerical methods share this single, conformal rectangular grid with embedded fractures

for both mechanical deformation and fluid-flow problems. With hybrid continuum models, a highly refined mesh is not necessary in order to obtain accurate strain/stress and pressure fields. The MINC concept allows the hybrid model to handle the extreme contrast in conductivity between the small-scale fracture network and the ultratight matrix that results in steep potential gradients.

The strain-stress relationship in multi-porosity media is used as a constitutive equation for coupling flow and rock mechanics. Moreover, assuming proppant preexists in the system, a proppant model is proposed to consider the influence on the fracture aperture.

We validate the accuracy of our approach using Mandel's Problem and a pure mechanics single fracture problem. We present simulation results for scenarios with multiple fractures.

ACKNOWLEDGEMENTS

First and foremost, I would like to express my sincere thanks to my advisor, Dr. Rami Younis, who has always been consistent in guiding me. During my study at TU, I have benefited tremendously from his thoughtful guidance and insightful suggestions. Dr. Younis has been a consistent source of knowledge, advice and encouragement, not only in my research work, but also in my personal life.

I would also like to thank other members of my dissertation committee, Dr. Albert C. Reynolds and Dr. Michael Keller, for their time and effort to serve on my committee and review my dissertation.

I owe my gratitude to the Department of Petroleum Engineering, all the faculty, staff, and my fellow students. They have made my years at TU inspiring and rewarding. Their great help and friendship are very much appreciated.

I would like to express my deepest gratitude to my parents for their endless love, support, and encouragement throughout my graduate study at TU. My achievements would not have been possible without their help and inspiration.

TABLE OF CONTENTS

COPYRIGHT STATEMENT	iii
ABSTRACT	iv
ACKNOWLEDGEMENTS	vi
TABLE OF CONTENTS	vii
LIST OF FIGURES	ix
LIST OF TABLES	xi
CHAPTER 1: INTRODUCTION	1
1.1 Literature Review	1
1.2 Outline	6
CHAPTER 2: POROMECHANICS DEFORMATION	7
2.1 Theory of Linear Elastic Fracture Mechanics	7
2.2 Force Equilibrium Equation	12
2.3 Dual Porosity	13
2.4 Proppant Model	15
2.5 Introduction to XFEM	18
2.6 Weak Form and coupled XFEM with Dual Porosity Discretization	23
2.6.1 <i>Weak Form</i>	23
2.6.2 <i>Discretization</i>	24
2.6.3 <i>Numerical Integration</i>	26
CHAPTER 3: FLUID FLOW MODELS	29
3.1 Governing Equation for Single Fluid Flow	29
3.2 EDFM Model	32
3.3 Dual Continuum Model	34
3.3.1 <i>Shape Factor</i>	36
3.4 Geomechanical Effects on Porosity and Permeability	38
3.4.1 <i>Geomechanical Effects on the Properties of Dual Continua</i>	38
3.4.2 <i>Geomechanical Effects on Hydraulic Fracture Permeability</i>	40
3.5 Discretization	40
3.6 Solution Algorithm	43
CHAPTER 4: NUMERICAL CASES	45

4.1	Mandel's Problem	45
4.2	Single Fracture Mechanics	48
4.3	Convergence Analysis	52
4.4	Synthetic Field Examples	55
4.4.1	<i>Effects of Natural Fracture Properties on the Coupled System</i>	55
4.4.2	<i>Effects of Proppant Properties on the Coupled System</i>	59
CHAPTER 5: CONCLUSIONS		64
BIBLIOGRAPHY		65

LIST OF FIGURES

2.1 Stress components on an infinitesimal material element.....	8
2.2 A biaxially loaded infinite plate containing a crack	9
2.3 The polar coordinate system associated with the crack tip.....	11
2.4 A body in a state of elastostatic equilibrium.....	12
2.5 Schematic of the dual porosity system.....	14
2.6 Initial and deformed configuration of proppants in the discretized fracture (2D).....	17
2.7 Different types of elements and nodes.....	19
2.8 Schematic of the signed distance function.....	20
2.9 Standard shape functions for nodes 2 and 3.....	22
2.10 Enriched shape functions for nodes 2 and 3	22
2.11 Shifted enriched functions for nodes 2 and 3.....	22
2.12 Partitioning of the element with sub triangles	26
2.13 Integration points in a singular element (Fries and Belytschko, 2010)	28
3.1 An idealized sugar cube of a fractured reservoir (Warren and Root 1963).....	35
3.2 Schematic of fracture aperture change due to strain.....	39
4.1 Illustration of Mandel's problem	45
4.2 Mandel's problem validation	47
4.3 Schematic of a center crack in a infinite plane	48
4.4 Crack opening displacement versus X coordinates on fracture	49
4.5 Element selected (dark grids) near the crack tip for the J integral.....	50
4.6 Inclined crack stress intensify factor	51

4.7 A schematic of a single hydraulic fracture in the unconventional reservoir.....	52
4.8 Error in pressure versus number of grid blocks	54
4.9 Error in displacement versus number of nodes	54
4.10 A schematic of a hydraulically fractured unconventional reservoir	56
4.11 Natural fracture aperture changes at $t = 200$ days.....	57
4.12 Gas production rate versus time.....	59
4.13 A schematic of a hydraulically fractured unconventional reservoir	60
4.14 Hydraulic fracture aperture after production for 1000 days	62
4.15 Gas production rate versus time.....	63

LIST OF TABLES

4.1 Input parameter for Mandel's problem	47
4.2 Normalized values of the stress intensity factors.....	51
4.3 Parameters for grid refinement	53
4.4 Hydraulic fracture position information	61

CHAPTER 1

INTRODUCTION

1.1 Literature Review

Reservoir geomechanics plays an important role in the analysis of phenomena, such as subsidence, primary compaction drive, hydraulic fracturing, and wellbore stability. In particular, the quantification of the state of deformation and stress in the reservoir is essential for the accurate prediction of flow-related phenomena (Jha and Juanes, 2007). Numerous studies have been reported on the simulation of coupled flow and geomechanics in conventional (unfractured) reservoirs (Tran et al., 2002; Thomas et al. 2002; Chin et al., 1998; Jha and Juanes, 2007). Unconventional reservoirs are becoming increasingly important oil and gas resources in the United States. Unconventional reservoirs are comprised of an ultra-low permeability fractured matrix that may consist of multiple continua. Natural fractures form highly connected networks with a wide range of length scales. The natural fractures are primarily supported by pore pressure. Horizontal wells are stimulated by hydraulic fractures that emanate from the wellbore along clusters within multiple stages. The hydraulic fractures are supported by pore pressure as well as by the pressure of proppants that are delivered during the completion process. Empirical observations from field practice suggest that geomechanical effects may play a first-order role in production from unconventional reservoirs. It is frequently observed that the production rate in tight gas reservoirs declines rapidly in a manner that is believed to be closely related to the evolution of the fracture aperture and permeability with time (Huang

and Ghassemi, 2012). Therefore, in order to accurately model such systems, it is necessary to couple flow and geomechanics, thereby capturing the influence of rock deformation and fracture aperture changes on field properties such as porosity and permeability.

The fundamentals of geomechanics are based on the concept of effective stress that was formulated by Terzaghi (Skempton, 1960) and Biot (1941). Terzaghi first proposed the relationship for effective stress in a one dimensional case (Skempton, 1960). Later, Biot formulated the quasi-static constitutive equations that relate the strain tensor linearly to both the stress tensor (Berryman and Wang, 1995) and the fluid pressure. Subsequently a generalized theory of three-dimensional consolidation was developed. However, in a reservoir where fractures are present, Biot's poroelastic theory of single porosity is no longer applicable. In order to characterize flow and deformation in fractured reservoirs, Barenblatt first introduced the dual-porosity/dual-permeability concept. In dual porosity theory, the rock and fractures are represented by two different interacting continua. Typically, the rock continuum is entirely surrounded by a thin layer of a fracture continuum. Bai (1999) offered a more rigorous physical interpretation of dual porosity poroelasticity (DPP). Two separate effective stress laws are applied in order to capture different extents of deformation of matrices and fractures. Berryman and Wang (1995) proposed a set of physical experiments to interpret the linear constitutive parameters in the dual porosity model. Later, Berryman (2002) determined those parameters in a more elegant fashion using a new self-similar thought experiment. Kim (2012) extended the dual porosity model reported by Berryman to the multiple interacting continua method (MINC) using the same idea of self-similar thought experiment in order to determine coefficients of multiple porosity systems. Kim applied the MINC idea to simulate fluid flow with

chemical reactions in fractured geothermal reservoirs (Kim, 2015). Another dual continuum concept (the dual permeability method) has been used for coupled flow and geomechanics (Huang and Ghassemi 2012; Wei and Zhang; 2010). The existing dual porosity approaches average fractures out and lose fracture information such as length, orientation and aperture.

Another category of coupled flow and geomechanics models treats fractures explicitly. Numerous numerical approaches that explicitly deal with fractures in coupled flow and geomechanics have been proposed. In all of these methods, fractures are represented in a lower dimension. For example, in three-dimensional domains, the fractures are described as two-dimensional surfaces. Levonyan (2011), Monteagudo et al. (2011), Garipov et al. (2014) and Karimi-Fard et al. (2003) employ a discrete fracture model (DFM) for flow, and a single static unstructured grid is used to represent all the fractures as lower-dimensional objects that are embedded within the matrix. In order to capture the poromechanical deformation, the mesh nodes are duplicated on the fractures (element interfaces) because additional degrees of freedom are needed. A good mesh generator which can handle very complicated geometries is necessary. These approaches are only suitable for problems where fractures are static, since otherwise, remeshing and complicated post processing would be needed at each time step.

Semi-analytical methods to model fracture mechanics include the boundary element method (BEM) and the displacement discontinuity method (DDM). DDM is a special case of BEM and was developed by Crouch (1976). DDM is designed to handle problems with crack-like geometries. Wu (2015) applied DDM to model hydraulic fractures and horizontal wells assuming that the fractures are embedded in an elastic

domain, and flow only occurs in fractures. McClure and Horne (2010) used DFM for flow and DDM for mechanics in order to simulate naturally fractured reservoirs. While their model considers flow in the porous medium, it assumes that the fracture deformation does not affect the matrix fluid pressure and the changes in the matrix fluid pressure do not affect the stress on fractures (McClure, 2015). Ganis et al. (2013) utilized the symmetric Galerkin boundary element method (SGBEM) coupled with the finite element method to capture the deformation of porous media. Nevertheless, the error in this method is small only when domain size is large and fractures are not close to the boundary. A variational approach to solving fracture problems was recently proposed. Bourdin et al. (2012) formulated a phase field method for hydraulic cracks in an elastic domain. Singh et al. (2014) and Wick et al. (2015) extended the phase field method to account for the poroelastic nature of the rock and studied linear fracture propagation. With the phase-field approach, a lower-dimensional crack surface is approximated as a diffusive transition zone characterized by a band width and a phase-field function (Wick et al., 2015). The phase field method avoids relying on a mesh generator and is able to handle complex fracture patterns. In recent years, the extended finite element method (XFEM) (Moës et al., 1999, Belytschko, 2001) has been successfully implemented for linear elastic fracture mechanics and propagation. XFEM does not need the fracture to be aligned with the mesh and can achieve good accuracy without requiring a highly refined mesh. Lamb et al. (2010) developed a model that coupled XFEM with the dual permeability method for poroelastic medium.

In this thesis, a fully coupled XFEM-EDFM with a dual porosity hybrid model is proposed to accurately simulate displacement and stress fields and fluid flow in fractured reservoirs. EDFM is used to describe the fluid flow interaction between the porous matrix

and primary fractures, while XFEM is used to address the discontinuous displacement field within elements that intersect fractures. The dual porosity concept allows the hybrid model to handle the small-scale fracture network around primary fractures in SRV. The proposed hybrid method includes the effect of each hydraulic fracture explicitly without requiring the simulation mesh to conform to the fracture geometry and also avoids explicit representation of natural fracture networks. Thus the challenges of high computational cost and the need for a complex meshing technique associated with UDFM are overcome.

To date, the effect of proppants on the system has not been addressed. A proppant model is proposed to simulate production from hydraulic fractures. The natural fractures are predominantly supported by pore pressure. The coupled system of nonlinear equations, boundary conditions and associated constitutive relations are solved using a fully implicit method to ensure stability.

1.2 Outline

In Chapter 2, the theory of linear fracture elastic fracture mechanics is reviewed, and the governing equation for poromechanical deformation is described. This is followed by an introduction to the dual porosity model to capture the deformation of fine-scale natural fractures. An extended finite element method combined with a proppant model is also proposed to predict the hydraulic fracture aperture change and the proppant deformation in hydraulic fractures. The weak form of the governing equation and finite element discretization are also presented.

In Chapter 3, the governing equations for fluid flow are introduced. Then, the EDFM and dual porosity models are described along with the solution algorithm that is applied to the coupled system.

In Chapter 4, we verify our model by comparison to analytical solutions. The impact of dual porosity and proppant mechanical properties on production is analyzed.

Chapter 5 concludes the thesis with a summary of accomplishments and recommendations for future work.

CHAPTER 2

POROMECHANICS DEFORMATION

The objective of this chapter is to develop the weak form of the coupled XFEM-EDFM with dual porosity model including proppants. The Galerkin method is applied to formulate a discretization of the weak form.

2.1 Theory of Linear Elastic Fracture Mechanics

Linear elastic theory predicts that stress at the tip of the crack tends to the infinity. Griffith (1921) first formulated a crack propagation criterion for brittle materials and succeeded in finding the relationship between crack size and fracture strength. Later, Griffith's theory was modified, and the concept of the stress intensity factor (SIF) and energy release rate were introduced. Westergaard (1939) proposed an Airy function as a solution to the crack problem in two dimensions.

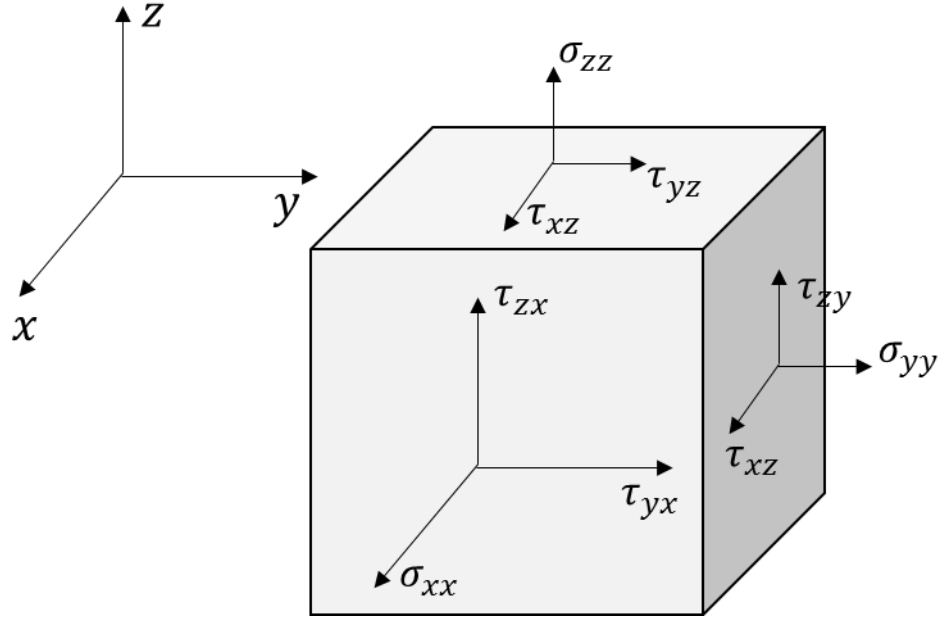


Figure 2.1 Stress components on an infinitesimal material element

Next, we introduce the stress equilibrium equations. From Figure. 2.1, the equation for equilibrium in the x direction can be written as

$$\left(\sigma_x + \frac{\partial \sigma_x}{\partial x} dx\right) dydz - \sigma_x dydz + \left(\tau_{xy} + \frac{\partial \tau_{xy}}{\partial y} dy\right) dzdx - \tau_{xy} dx dz + \left(\tau_{xz} + \frac{\partial \tau_{xz}}{\partial z} dz\right) dx dy - \tau_{xz} dx dy = 0. \quad (2.1)$$

We can write the similar forms in the y and the z direction under the quasi-static state,

$$\frac{\partial \sigma_x}{\partial x} + \frac{\partial \tau_{xy}}{\partial y} + \frac{\partial \tau_{xz}}{\partial z} = 0, \quad (2.2a)$$

$$\frac{\partial \sigma_y}{\partial y} + \frac{\partial \tau_{yz}}{\partial z} + \frac{\partial \tau_{xy}}{\partial x} = 0, \quad (2.2b)$$

and

$$\frac{\partial \sigma_z}{\partial z} + \frac{\partial \tau_{zx}}{\partial x} + \frac{\partial \tau_{zy}}{\partial y} = 0. \quad (2.2c)$$

In the two-dimensional case, Eq. (2.2) could be reduced to

$$\frac{\partial \sigma_x}{\partial x} + \frac{\partial \tau_{xy}}{\partial y} = 0 \quad (2.3a)$$

and

$$\frac{\partial \sigma_y}{\partial y} + \frac{\partial \tau_{xy}}{\partial x} = 0. \quad (2.3b)$$

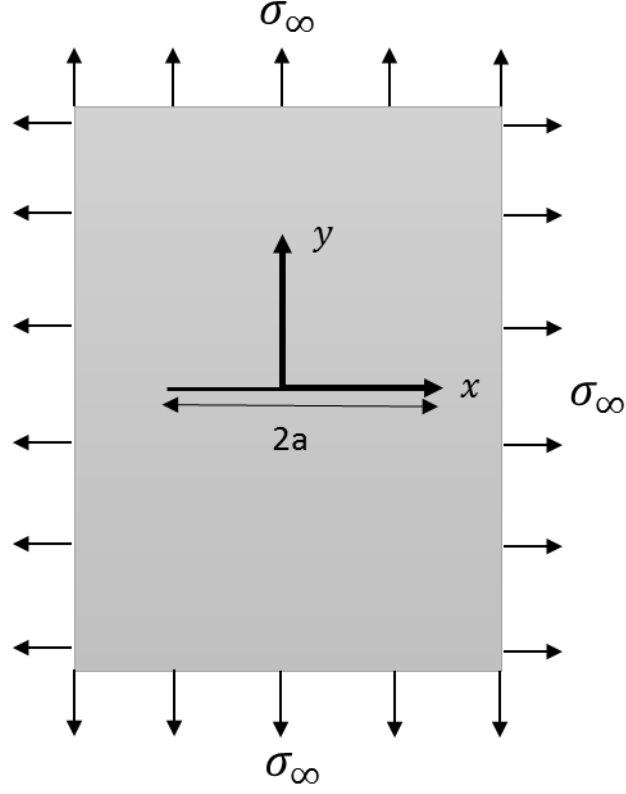


Figure 2.2 A biaxially loaded infinite plate containing a crack

Now, we can solve the problem of biaxially loaded plate with a central crack in Figure. 2.2. The governing equation is Eq. (2.3), and the boundary conditions are

$$\sigma_y = 0 \quad -a < x < +a \text{ and } y = 0, \quad (2.4)$$

$$\sigma_x = \sigma_\infty, \sigma_y = \sigma_\infty \quad x \rightarrow \pm\infty \text{ and } y \rightarrow \pm\infty, \quad (2.5)$$

and

$$\sigma_y = \infty \quad x = \pm a \text{ and } y = 0. \quad (2.6)$$

Westergaard introduced a specific type of Airy stress function, Φ , using an analytical complex stress function, $\phi(z)$, which has its first and second order integrals

$$\Phi = \text{Re}\bar{\bar{\phi}}(z) + y \cdot \text{Im}\bar{\phi}(z), \quad (2.7)$$

where $\bar{\phi}(z)$ is the first order integral of $\phi(z)$, $\bar{\bar{\phi}}$ is the second order integral of $\phi(z)$, and $z = x + iy$.

The Airy stress functions give us

$$\sigma_x = \frac{\partial^2 \Phi}{\partial y^2}, \sigma_y = \frac{\partial^2 \Phi}{\partial x^2}, \tau_{xy} = -\frac{\partial^2 \Phi}{\partial x \partial y}, \quad (2.8)$$

and if we substitute Eq. (2.7) into Eq. (2.8), we obtain the following expressions for stress:

$$\sigma_x = \text{Re}\phi(z) - y \cdot \text{Im}\phi'(z), \quad (2.9)$$

$$\sigma_y = \text{Re}\phi(z) + y \cdot \text{Im}\phi'(z), \quad (2.10)$$

and

$$\tau_{xy} = -y \cdot \text{Re}\phi'(z). \quad (2.11)$$

In the region near the crack tip, the above solution can be simplified:

$$\sigma_x = \frac{\sigma\sqrt{\pi a}}{\sqrt{2\pi r}} \cos \frac{\theta}{2} \left(1 - \sin \frac{\theta}{2} \sin \frac{3\theta}{2}\right), \quad (2.12)$$

$$\sigma_y = \frac{\sigma\sqrt{\pi a}}{\sqrt{2\pi r}} \cos \frac{\theta}{2} \left(1 + \sin \frac{\theta}{2} \sin \frac{3\theta}{2}\right), \quad (2.13)$$

and

$$\tau_{xy} = \frac{\sigma\sqrt{\pi a}}{\sqrt{2\pi r}} \sin \frac{\theta}{2} \cos \frac{\theta}{2} \cos \frac{3\theta}{2}, \quad (2.14)$$

where r, θ are under the local polar system located at the crack tip. Figure. 2.3 shows the polar system at the crack tip.

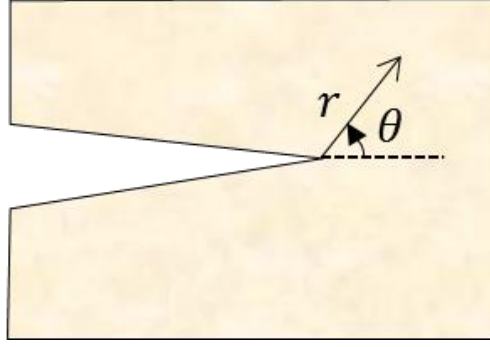


Figure 2.3 The polar coordinate system associated with the crack tip

A function that satisfies the equilibrium equations and the boundary conditions is

$$\phi = \frac{\sigma_{\infty}}{\sqrt{1 - \frac{a^2}{z^2}}}, \quad (2.15)$$

where a is the half crack length.

We can also obtain a useful expression for the crack opening displacement in two-dimensional domains as

$$\text{COD} = \frac{2\sigma_{\infty}}{E'} \sqrt{a^2 - x^2}, \quad (2.16)$$

where $E' = E$ in the plane stress condition, $E' = \frac{E}{1-\nu^2}$ in the plane strain condition, E is Young's modulus, and ν is the Poisson's ratio.

2.2 Force Equilibrium Equation

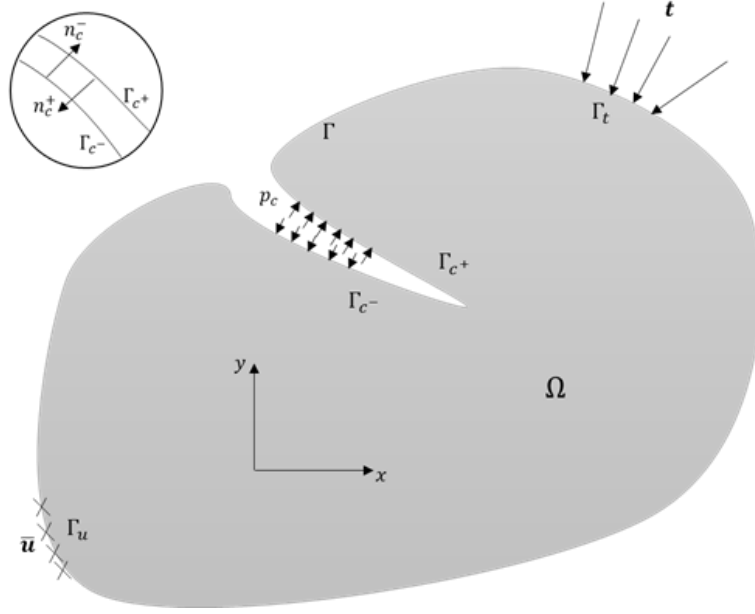


Figure 2.4 A body in a state of elastostatic equilibrium

Figure. 2.4 shows a body with a fracture under equilibrium state. \mathbf{n}_t is the unit outward normal vector to the external boundary, \mathbf{t} is the prescribed traction applied to the boundary, and $\bar{\mathbf{u}}$ is prescribed displacement on the external boundary. On the inner fracture boundary Γ_c , the fracture pore pressure, p_c , is exerted on the fracture inner faces. The two unit outer normal vectors on the two fracture faces are \mathbf{n}_c^+ and \mathbf{n}_c^- .

The governing equation for poromechanics under the quasi-static assumption is

$$\nabla \cdot \boldsymbol{\sigma} + \rho_b \mathbf{g} = 0, \quad (2.17)$$

where $\boldsymbol{\sigma}$ is the Cauchy total stress tensor and ρ_b is the bulk density.

The boundary conditions are

$$\boldsymbol{\sigma} \cdot \mathbf{n}_t = \mathbf{t} \text{ on } \Gamma_t, \quad (2.18a)$$

$$\mathbf{u} = \bar{\mathbf{u}} \text{ on } \Gamma_u, \quad (2.18b)$$

and

$$\boldsymbol{\sigma} \cdot \mathbf{n}_c^- = -\boldsymbol{\sigma} \cdot \mathbf{n}_c^+ = -p_c \mathbf{n}_c^+ = p_c \mathbf{n}_c^- = p_c \mathbf{n}_c = \bar{\mathbf{p}} \text{ on } \Gamma_c. \quad (2.18c)$$

Here we make the assumption of infinitesimal transformation, and it follows the strain tensor is defined as the symmetric gradient of the displacement:

$$\boldsymbol{\varepsilon} = \frac{1}{2}(\nabla \mathbf{u} + \nabla^T \mathbf{u}) \quad (2.19)$$

and the volumetric strain is $\epsilon_v = \text{trace}(\boldsymbol{\varepsilon})$.

2.3 Dual Porosity

Natural fractures near hydraulic fractures have a significant impact on increasing the mobility of fluid in the reservoir. However, treating complicated natural fracture patterns explicitly by EDFM and XFEM is difficult and computationally expensive. In characterizing flow and deformation between matrix and fractures, an extension from a single porosity (Biot, 1957) to a dual porosity concept (Barenblatt, 1960) is applied in order to addressing the problem. DPP (Bai, 1999) which has a rigorous physical interpretation of the dual porosity model, is implemented in the simulator.

In Bai's model, instead of using only one effective stress law (Wilson and Aifantis, 1982), two separate effective stress laws for fracture and matrix are assumed:

$$\boldsymbol{\sigma}_m = \boldsymbol{\sigma}'_m - \alpha_m p_m \mathbf{I} \quad (2.20a)$$

and

$$\boldsymbol{\sigma}_f = \boldsymbol{\sigma}'_f - \alpha_f p_f \mathbf{I}, \quad (2.20b)$$

where $\boldsymbol{\sigma}_m$ is the matrix total stress, $\boldsymbol{\sigma}_f$ is the fracture total stress, $\boldsymbol{\sigma}'_m$ is the matrix effective stress, $\boldsymbol{\sigma}'_f$ is the fracture effective stress, α_m is the matrix Biot's coefficient, α_f is the fracture Biot's coefficient, and the Biot's coefficient has a value between porosity and unity.

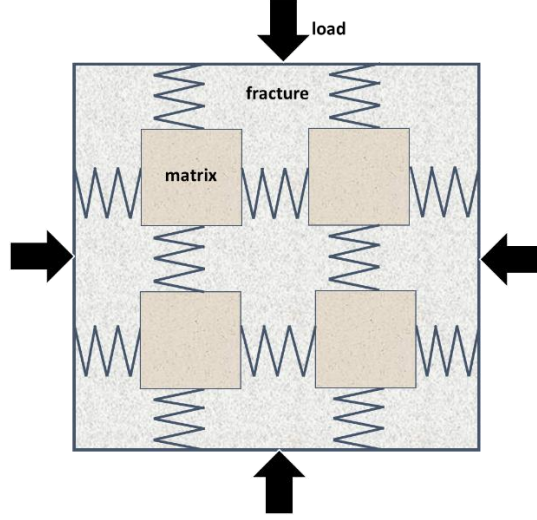


Figure 2.5 Schematic of the dual porosity system

The relationship between the matrix and fracture is depicted in Figure. 2.5. The model assumes that the matrix is surrounded by orthogonal intersecting fractures. After deformation, total stresses in each continuum are equal:

$$\boldsymbol{\sigma} = \boldsymbol{\sigma}_m = \boldsymbol{\sigma}_f. \quad (2.21)$$

However, total strains are summed from the two media:

$$\boldsymbol{\varepsilon} = \boldsymbol{\varepsilon}_m + \boldsymbol{\varepsilon}_f. \quad (2.22)$$

From Eqs. (2.20) to (2.22) and Hooke's Law, a modified effective stress law can be written:

$$\boldsymbol{\sigma} = D_{mf} : \boldsymbol{\varepsilon} - D_{mf} : C_m : \alpha_m p_m \mathbf{I} - D_{mf} : C_f : \alpha_f p_f \mathbf{I}, \quad (2.23)$$

where D_{mf} is a fourth order elastic stiffness tensor evaluated from properties of the matrix and fracture, C_m is the matrix compliance tensor, and C_f is the fracture compliance tensor. In this thesis, we assume linear elastic properties for both the matrix and fracture. For the two-dimensional case,

$$C_m = \frac{1}{E'} \begin{bmatrix} 1 & -\nu' & 0 \\ -\nu' & 1 & 0 \\ 0 & 0 & 1 + \nu' \end{bmatrix}, \quad (2.24)$$

where $E' = E$ and $\nu' = \nu$ for the plane stress condition, $E' = \frac{E}{1-\nu^2}$ and $\nu' = \frac{\nu}{1-\nu}$ for the plane strain condition, and

$$C_f = \frac{1}{S} \begin{bmatrix} \frac{1}{K_n} & 0 & 0 \\ 0 & \frac{1}{K_n} & 0 \\ 0 & 0 & \frac{1}{K_{sh}} \end{bmatrix}, \quad (2.25)$$

where S is fracture spacing.

For the convenience of derivation in the later part, we define the following variables:

$$\alpha_m^* = \alpha_m D_{mf} : C_m \quad (2.26a)$$

and

$$\alpha_f^* = \alpha_f D_{mf} : C_f. \quad (2.26b)$$

The advantage of the model is that it includes two sets of parameters of matrix and fracture. Consequently it considers the matrix and fracture deformation individually. Eq. (2.23) indicates that the integrated matrix and fracture system deforms in the same manner where ε is the total strain for the system. In the simulator, Eq. (2.23) is used as the effective stress law for dual porosity. After displacement fields are solved, strain for each continuum can be obtained from Eqs. (2.20) to (2.22).

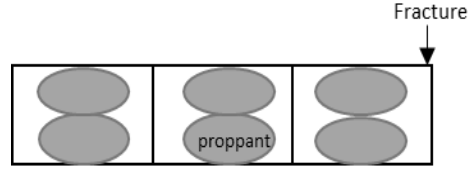
2.4 Proppant Model

Proppants in hydraulic fractures resist closure of fractures and play a significant role in the unconventional reservoir production. However, because of the interaction between proppants and hydraulic surfaces, proppants may be deformed, embedded or

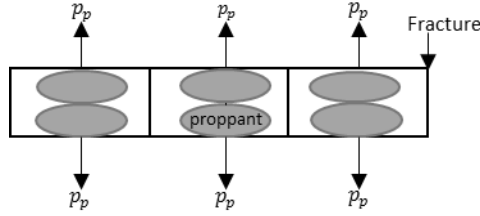
crushed in fractures. Numerous experimental and analytical studies have investigated these three factors (deformation, embedment and crush) causing reduction in fracture conductivity and production. (Mindlin and Deresiewicz, 2013; Huitt and Mcglothlin, 1958; Huiit et al., 1959; Volk et al., 1981; Guo, 2008; Lacy et al., 1998; Li et al., 2015). We obtain the following conclusions from the research mentioned above:

1. The condition of sand propping would crush rather than embed under the weight of overburden (Huiit et al., 1959).
2. Many factors such as rock property, proppant size and mechanical property, the concentration of proppant-paving could influence embedment of the proppant.
3. As the elastic modulus of coalbed (embedment surface) increases, the aperture change gradually approaches the proppant deformation, and the proppant embedment approaches zero (Li et al., 2015).

Only few research papers have numerically analyzed the proppant behavior in hydraulic fractures. Here we propose a simple proppant model for hydraulic fractures. We assume that no conductivity loss is caused by proppants and that the proppant obeys the linear elastic behavior. We also assume that the elastic modulus of the embedment surface is larger than that of proppants so that the reduction in the fracture aperture is mainly caused by proppant deformation. We define the force exerted on fracture faces by proppants as p_p .



(a) Initial



(b) Deformed

Figure 2.6 Initial and deformed configuration of proppants in the discretized fracture (2D)

During a production process, the decrease of hydraulic fracture pressure causes a tendency for the fracture to close. However, when proppants are present, deformed proppants will exert a force on fracture faces and resist closure. According to the Hooke's Law, the pressure p_p caused by proppants will be

$$p_p = \begin{cases} E_p \frac{-\mathbf{w} \cdot \mathbf{n}_c}{D_i} & \mathbf{w} \cdot \mathbf{n}_c < 0 \\ 0 & \text{otherwise,} \end{cases} \quad (2.27)$$

where E_p is the Young's modulus of proppants, \mathbf{w} is the fracture opening displacement, and D_i is the initial fracture aperture. Eq. (2.27) shows that a proppant is only effective when a fracture aperture is being decreased.

2.5 Introduction to XFEM

In order to model discontinuity fields, enriched basis FEM is commonly applied. The enrichment is realized through the basic mathematical foundation of the partition of unity finite element method (PUFEM) as proposed by Melenk and Babuška (1996). The global solution of PUFEM has been the theoretical basis of the extended finite element method.

XFEM has many advantages. One new feature of XFEM is that only local parts of the domain are enriched and this localization is achieved by enriching a subset of nodes (Moës et al., 1999). The cost of computation is reduced significantly because of the localized enrichment. Moreover, more complicated physical phenomenon are also easier to simulate by means of XFEM. Because fractures are represented independently from the mesh, no remeshing is required when fracture propagation is involved. Moreover, it is easy to extend to heterogeneous or even nonlinear mechanical property problems.

In Figure. 2.7, different types of elements (standard, blending, enriched) and nodes (standard, Heaviside enriched, Tip function enriched) are shown. In the standard and enriched elements, a partition of unity is satisfied. The blending element is no longer a partition of unity. Nevertheless, it has little direct effect on the approximation because a blending element does not include a singularity. The appearance of blending elements especially for those near fracture tips could decrease the convergence rate of XFEM (Fries and Belytschko, 2010).

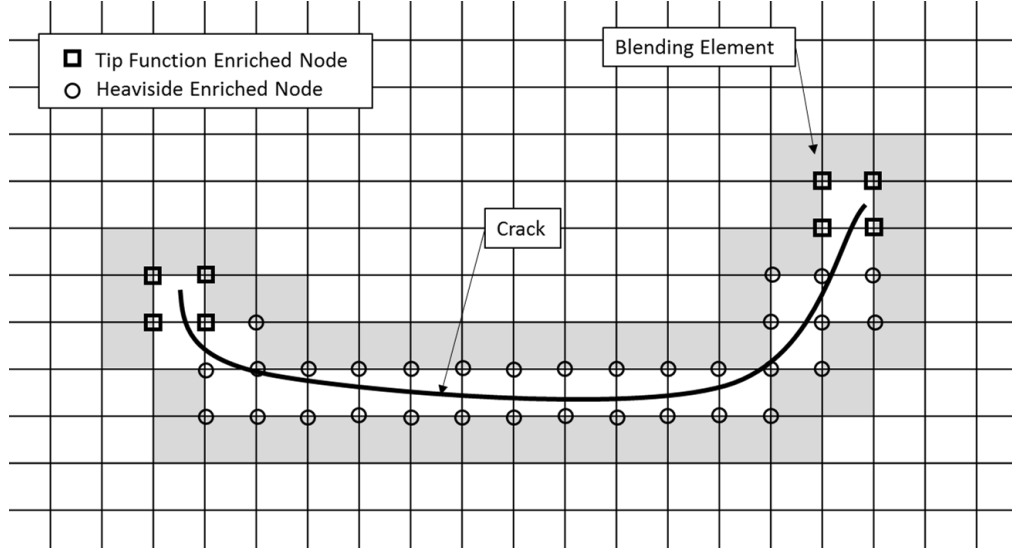


Figure 2.7 Different types of elements and nodes

For XFEM, Moës et al. (1999) proposed an equation that can model crack surfaces and tips by step functions and asymptotic near-tip fields. The finite element approximation for a single crack in a two-dimensional body can be written as

$$\mathbf{u}^h(\mathbf{x}) = \sum_{i \in I} N_i(\mathbf{x}) \mathbf{u}_i + \sum_{i \in L} N_i(\mathbf{x}) H(\xi(\mathbf{x})) \mathbf{a}_i + \sum_{i \in K_1} N_i(\mathbf{x}) \left(\sum_{l=1}^4 F_l(\mathbf{x}) \mathbf{b}_{i,1}^l \right) + \sum_{i \in K_2} N_i(\mathbf{x}) \left(\sum_{l=1}^4 F_l(\mathbf{x}) \mathbf{b}_{i,2}^l \right), \quad (2.28)$$

where I is the set of all nodes in the mesh, \mathbf{u}_i is the classical degree of freedom at node i , N_i is the shape function associated with node i , $L \subset I$ is the subset of nodes that are enriched for the crack discontinuity, and \mathbf{a}_i correspond to additional degrees of freedom. The nodes in L are such that their support (elements that are connected by a node) intersects the crack but does not contain any of its crack tips. The subsets $K_1 \subset I$ and $K_2 \subset I$ are the sets of nodes that are enriched for the first and second crack tips, respectively. The corresponding additional degrees of freedom are $\mathbf{b}_{i,1}^l$ and $\mathbf{b}_{i,2}^l$, $l = 1, \dots, 4$, for the first and second crack tip, respectively.

An illustration of the signed distance function is shown in Figure. 2.8, and its definition is

$$\xi(\mathbf{x}) = \min \|\mathbf{x} - \mathbf{x}_\Gamma\| \text{sign}(\mathbf{n} \cdot (\mathbf{x} - \mathbf{x}_\Gamma)), \quad (2.29)$$

where \mathbf{x}_Γ is a projection of \mathbf{x} onto an arbitrary surface, and \mathbf{n} is the unit outward normal vector of the surface.

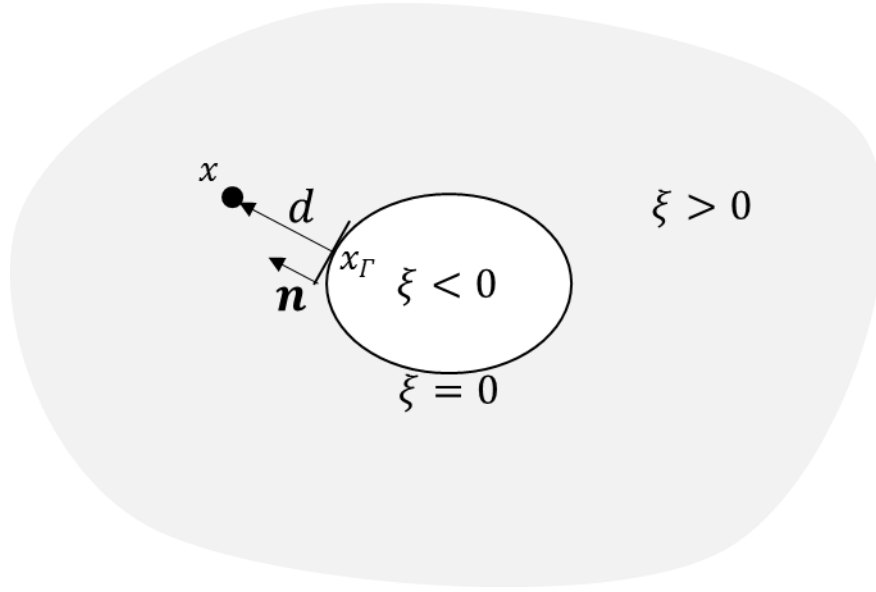


Figure 2.8 Schematic of the signed distance function

The Heaviside distribution is defined by,

$$H(\xi) = \begin{cases} 1 & \forall \xi > 0 \\ 0 & \forall \xi = 0 \\ -1 & \forall \xi < 0. \end{cases} \quad (2.30)$$

The near tip enrichment functions have already been defined in terms of a local crack tip coordinate system (r, θ) . Note that only the first function in Eq. (2.31) is discontinuous across the surface $(\pm\pi)$, whereas the other three functions are continuous.

$$F_l(r, \theta) = \left\{ \sqrt{r} \sin \frac{\theta}{2}, \sqrt{r} \cos \frac{\theta}{2}, \sqrt{r} \sin \theta \sin \frac{\theta}{2}, \sqrt{r} \sin \theta \cos \frac{\theta}{2} \right\}. \quad (2.31)$$

To model the discontinuity, virtual nodes are imposed onto standard nodes and are combined with the classical finite element method to approximate a displacement field. In order to clarify how this method works, we illustrate it through a one dimensional problem that consists of four nodes and three elements with a strong discontinuity. There is a discontinuity between node 2 and 3. In Figure. 2.10 and Figure. 2.11, the approximation function at the left and right discontinuity points is totally different. If the approximation function is added to standard finite element shape functions, a discontinuous displacement field will be obtained. We also notice that the displacement at each node, in Figure. 2.10, is

$$\mathbf{u}^h = \mathbf{u}_i + H(\xi_i)\mathbf{a}_i. \quad (2.32)$$

At each node, the displacement is not equal to \mathbf{u}_i , which does not satisfy the interpolation. However, in Figure. 2.11, the shift function will not cause any blending elements.

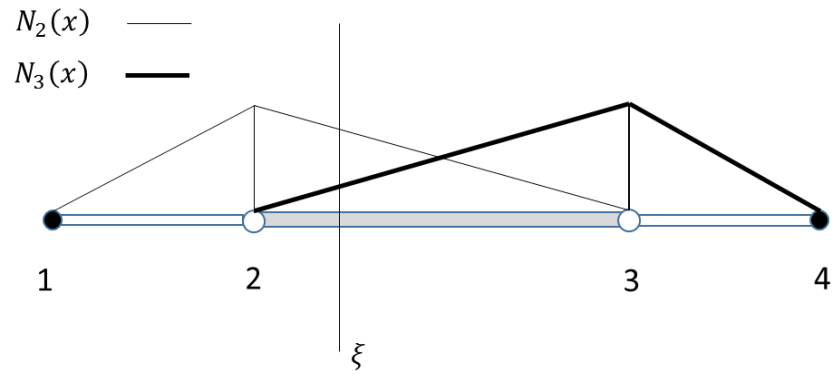


Figure 2.9 Standard shape functions for nodes 2 and 3

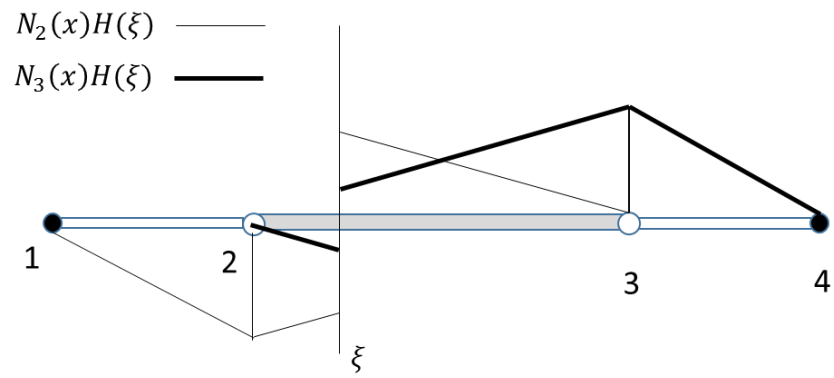


Figure 2.10 Enriched shape functions for nodes 2 and 3

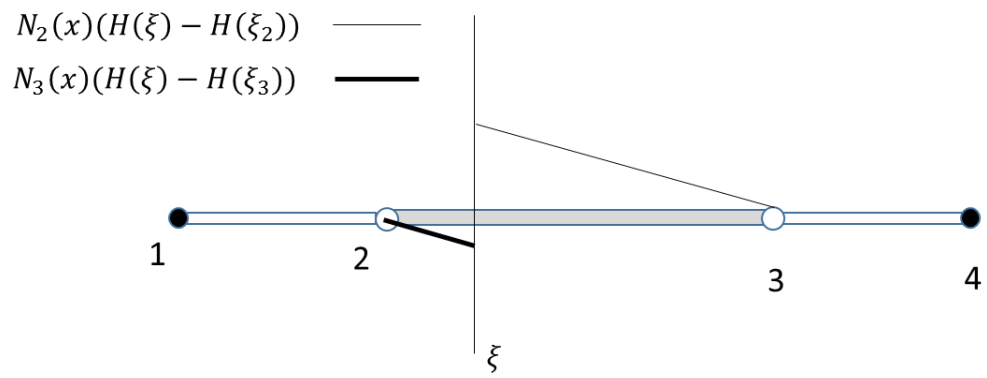


Figure 2.11 Shifted enriched functions for nodes 2 and 3

2.6 Weak Form and Coupled XFEM with Dual Porosity Discretization

2.6.1 Weak Form

The weak form of the equilibrium equation (neglecting body forces) is given by Chen (2013), Khoei (2014) and Mohammadi (2008). Here it is extended to include dual porosity and proppant models.

The space of the admissible solution for the displacement \mathbf{u} is defined as

$$\mathcal{U} = \{\mathbf{v} \in \mathcal{V}, \mathbf{v} = \bar{\mathbf{u}} \text{ on } \Gamma_u, \mathbf{v} \text{ discontinuous on } \Gamma_c\}, \quad (2.33)$$

where the space \mathcal{V} is related to the regularity of the solution in which \mathbf{v} is discontinuous over the fracture. The test function is defined similarly as

$$\mathcal{U}_0 = \{\mathbf{v} \in \mathcal{V}, \mathbf{v} = 0 \text{ on } \Gamma_u, \mathbf{v} \text{ discontinuous on } \Gamma_c\}. \quad (2.34)$$

The weak form is to find $\mathbf{u} \in \mathcal{U}$ such that the solution satisfies the equilibrium equation. The weak form is derived by the Galerkin method and is given by

$$\begin{aligned} \int_{\Omega} \delta \boldsymbol{\varepsilon} : D_{mf} : \boldsymbol{\varepsilon} d\Omega &= \int_{\Omega} \delta \boldsymbol{\varepsilon} : \alpha_m^* p_m \mathbf{I} d\Omega + \int_{\Omega} \delta \boldsymbol{\varepsilon} : \alpha_f^* p_f \mathbf{I} d\Omega + \int_{\Gamma_t} \delta \mathbf{u} \cdot \mathbf{t} d\Gamma_t \\ &+ \int_{\Gamma_c^+} (\delta \mathbf{u}^+ - \delta \mathbf{u}^-) \cdot \bar{\mathbf{p}} d\Gamma_c + \int_{\Gamma_c^+} (\delta \mathbf{u}^+ - \delta \mathbf{u}^-) \cdot \mathbf{p}_p d\Gamma_c, \end{aligned} \quad (2.35)$$

where $\delta \mathbf{u}$ is the virtual displacement, and $\delta \boldsymbol{\varepsilon}$ is the virtual strain. We assume that the matrix pore pressure, p_m , and natural fracture pressure, p_f , act only on the normal direction. The shear force on the matrix due to the fluid flow is neglected. On the outer boundary Γ_t , \mathbf{t} is applied. On the inner boundary or discontinuity boundary Γ_c^+ or Γ_c^- , \mathbf{u}^+ and \mathbf{u}^- are displacements on fracture upper and lower faces separately. Besides the fluid pressure, $\bar{\mathbf{p}}$, a proppant force, \mathbf{p}_p , is also considered, and it acts only where the fracture has a tendency to close.

The equation for the crack opening displacement can be written as,

$$\mathbf{w} = \mathbf{n}_c \cdot (\mathbf{u}^+ - \mathbf{u}^-) \mathbf{n}_c, \quad (2.36)$$

Eq. (2.35) can be simplified by substitution of Eq. (2.36). Then the equation will be

$$\begin{aligned} \int_{\Omega} \delta \boldsymbol{\varepsilon} : D_{mf} : \boldsymbol{\varepsilon} d\Omega &= \int_{\Omega} \delta \boldsymbol{\varepsilon} : \alpha_m^* p_m \mathbf{I} d\Omega + \int_{\Omega} \delta \boldsymbol{\varepsilon} : \alpha_m^* p_f \mathbf{I} d\Omega + \int_{\Gamma_t} \delta \mathbf{u} \cdot \mathbf{t} d\Gamma_t + \\ &\int_{\Gamma_c^+} \delta \mathbf{w} \cdot (\bar{\mathbf{p}} + \mathbf{p}_p) d\Gamma_c. \end{aligned} \quad (2.37)$$

2.6.2 Discretization

Using the standard Galerkin procedure to discretize the system results in a system of linear equilibrium equations:

$$\mathbf{K} \mathbf{u}^h = \mathbf{f}, \quad (2.38)$$

where \mathbf{K} is a global stiffness matrix, \mathbf{u}^h is degrees of freedom for both standard nodes and enriched nodes, and \mathbf{f} is the force vector. The stiffness matrix and force vector are assembled element by element. In each element, the local stiffness matrix, \mathbf{K}_e , and force, \mathbf{f}_e , have the following structures,

$$\mathbf{K}_e = \begin{pmatrix} K_{ij}^{uu} & K_{ij}^{ua} & K_{ij}^{ub} \\ K_{ij}^{au} & K_{ij}^{aa} & K_{ij}^{ab} \\ K_{ij}^{bu} & K_{ij}^{ba} & K_{ij}^{bb} \end{pmatrix}, \quad (2.39)$$

and

$$\mathbf{f}_e = (\mathbf{f}_i^u, \mathbf{f}_i^a, \mathbf{f}_i^{b_\alpha}), \quad (2.40)$$

where i and j are the node numbers which range from 1 to 4 in each element, α varies from 1 to 4, u is the standard node, a is the Heaviside node, b_α is the tip function enriched node. For a linear fracture, each node in the element with a fracture tip is enriched by four asymptotic functions Eq. (2.31).

In each element, the element stiffness matrix, \mathbf{K}_{ij}^{rs} , and force vectors, \mathbf{f}_i^u , \mathbf{f}_i^a , $\mathbf{f}_i^{b\alpha}$, are defined as

$$\mathbf{K}_{ij}^{rs} = \int_{\Omega_e} (\mathbf{B}_i^r)^T D_{mf} \mathbf{B}_j^s d\Omega_e \quad (r, s = u, a, b_\alpha) \quad (i, j = 1..4), \quad (2.41)$$

$$\mathbf{f}_i^u = \int_{\Gamma_t} N_i \mathbf{t} d\Gamma_t + \int_{\Omega_e} (\mathbf{B}_i^u)^T (\alpha_f^* p_f + \alpha_m^* p_m) d\Omega_e, \quad (2.42)$$

$$\mathbf{f}_i^a = \int_{\Gamma_t} N_i H \mathbf{t} d\Gamma_t + \int_{\Gamma_c} 2N_i (\bar{\mathbf{p}} + \mathbf{p}_p) d\Gamma_c + \int_{\Omega_e} (\mathbf{B}_i^a)^T (\alpha_f^* p_f + \alpha_m^* p_m) d\Omega_e, \quad (2.43)$$

$$\begin{aligned} \mathbf{f}_i^{b\alpha} = & \int_{\Gamma_t} N_i F_\alpha \mathbf{t} d\Gamma_t + \int_{\Gamma_c} 2N_i F_1(r, \theta = \pi) (\bar{\mathbf{p}} + \mathbf{p}_p) d\Gamma_c + \\ & \int_{\Omega_e} (\mathbf{B}_i^\alpha)^T (\alpha_f^* p_f + \alpha_m^* p_m) d\Omega_e, \end{aligned} \quad (2.44)$$

$$\mathbf{B}_i^u = \begin{bmatrix} N_{i,x} & 0 \\ 0 & N_{i,y} \\ N_{i,y} & N_{i,x} \end{bmatrix}, \quad (2.45)$$

$$\mathbf{B}_i^a = \begin{bmatrix} N_i[H(\xi) - H(\xi_i)]_{,x} & 0 \\ 0 & N_i[H(\xi) - H(\xi_i)]_{,y} \\ N_i[H(\xi) - H(\xi_i)]_{,y} & N_i[H(\xi) - H(\xi_i)]_{,x} \end{bmatrix}, \quad (2.46)$$

and

$$\mathbf{B}_i^{b\alpha} = \begin{bmatrix} [N_i(F_\alpha - F_{\alpha i})]_{,x} & 0 \\ 0 & [N_i(F_\alpha - F_{\alpha i})]_{,y} \\ [N_i(F_\alpha - F_{\alpha i})]_{,y} & [N_i(F_\alpha - F_{\alpha i})]_{,x} \end{bmatrix} \quad (\alpha = 1, 2, 3, 4), \quad (2.47)$$

where \mathbf{B}_i^u is the derivative matrix of the standard node shape function. \mathbf{B}_i^a is the derivative matrix of the Heaviside enrichment shape function. $\mathbf{B}_i^{b\alpha}$ is the derivative matrix of tip enrichment shape functions.

2.6.3 Numerical Integration

The Gauss quadrature rule is often successfully applied in order to perform numerical integration in the finite element implementation. For polynomial integrands, the Gauss quadrature rule is proven to be accurate. However, in the XFEM, we introduce linear discontinuous functions which include a Heaviside function and nonlinear, singular, and discontinuous functions which are the tip enrichment functions. Subsequently, a less accurate estimate is obtained without any special treatments. Next, we develop two different numerical integration schemes that are suitable for Heaviside enrichment and tip enrichment shape functions respectively.

For the element cut by a crack, Dolbow (1999) proposed two methods to overcome this integration difficulty. In the first method, an element that is cut by a fracture is subdivided into several sub triangles. The ordinary Gauss quadrature rule is performed on each sub triangle where the integrand is a continuous polynomial. The second approach is to subdivide elements into sub-quads. Compared to the second method, the first one should be more efficient and accurate.

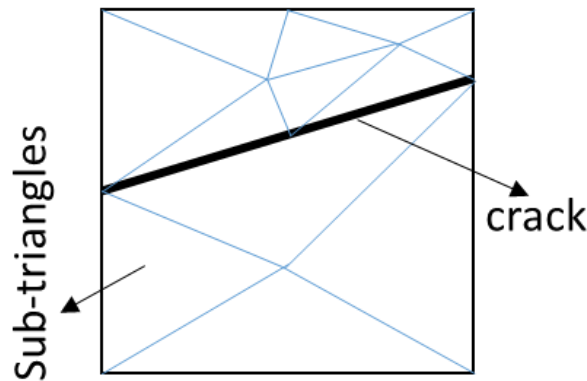


Figure 2.12 Partitioning of the element with sub triangles

For the element containing crack tips, the derivative of the tip enrichment shape functions will introduce a singularity term as well as a discontinuity. Thus a special quadrature rule is highly recommended for the singular integrand. Owing to high gradients near the singularity, a concentration of integration points in the vicinity of the singularity improves the results significantly. A numerical integration procedure is listed below:

1. An element is subdivided into sub-triangles.
2. A tensor product-type Gaussian quadrature rule is applied to each sub-triangular element.
3. The integration values from each sub element are summed.

The key idea of the tensor product-type Gaussian quadrature rule is to transform the standard triangular element T_{st} to the standard quadrilateral element R_{st} and then to apply the Gaussian quadrature rule for R_{st} . The advantage of this method is that the location of the Gauss points is concentrated on a relatively small region near one vertex. Figure 2.13 illustrates the process of numerical integration for elements containing tips.

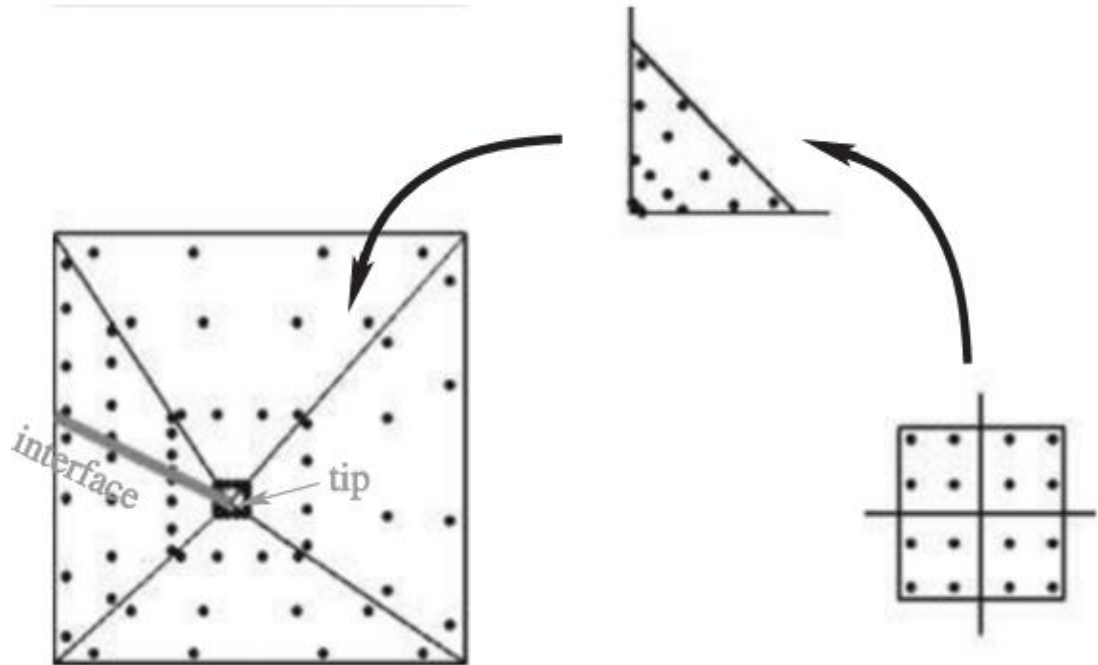


Figure 2.13 Integration points in a singular element (Fries and Belytschko, 2010)

CHAPTER 3

FLUID FLOW MODELS

In this chapter, we derive mass balance equations for two phase flow of black oil in deformable porous media. The development of governing equations is based on the following general assumptions:

1. Rock behaves as isothermal and obeys linear poroelasticity.
2. The geomechanical process is under a quasi-static equilibrium.
3. The deformation of porous media is infinitesimal.

We will introduce the EDFM and dual porosity models for the fluid flow. In the following poromechanics equations, the sign convention is adopted as positive for tension and negative for compression.

3.1 Governing Equation for Single Fluid Flow

The primary variables in the resulting system of governing equations are the fluid pressure (p) and the displacement (u). First we derive a single phase flow equation in deformable porous media.

Mass conservation of the solid phase is

$$\frac{\partial \rho_s(1-\phi)}{\partial t} + \nabla \cdot (\rho_s(1-\phi)V^s) = 0. \quad (3.1)$$

Mass conservation of the fluid phase is

$$\frac{\partial \rho_f \phi}{\partial t} + \nabla \cdot (\rho_f \phi V^f) = 0, \quad (3.2)$$

where ρ_α is the phase density, ϕ is the porosity, \mathbf{V}^α is the phase velocity, and $\alpha \in \{s, f\}$ denotes either solid or fluid phase.

The fluid equation is rewritten in terms of the solid phase velocity, and it gives

$$\frac{\partial \rho_f \phi}{\partial t} + \nabla \cdot (\rho_f \phi \mathbf{V}^s) + \nabla \cdot (\rho_f \phi (\mathbf{V}^f - \mathbf{V}^s)) = 0 \quad (3.3)$$

and the third term in Eq. (3.3) on the left can be replaced by the Darcy's velocity,

$$\frac{\partial \rho_f \phi}{\partial t} + \rho_f \phi \nabla \cdot (\mathbf{V}^s) + \mathbf{V}^s \cdot \nabla (\rho_f \phi) + \nabla \cdot (\rho_f \mathbf{V}^D) = 0. \quad (3.4)$$

Now, we define the material derivative as

$$\frac{D(\cdot)}{Dt} = \frac{\partial(\cdot)}{\partial t} + \mathbf{V}^s \cdot \nabla(\cdot). \quad (3.5)$$

We can write Eq. (3.4) in terms of using the material derivative, as

$$\frac{D(\rho_f \phi)}{Dt} + \rho_f \phi \nabla \cdot (\mathbf{V}^s) = -\nabla \cdot (\rho_f \mathbf{V}^D) \quad (3.6)$$

and Eq. (3.1) follows the same procedure:

$$\nabla \cdot \mathbf{V}^s = -\frac{1}{(1-\phi)\rho_s} \frac{D(1-\phi)\rho_s}{Dt}. \quad (3.7)$$

If we assume a constant solid mass ($D(\rho_s V_s) = 0$) and use $\phi = \frac{V_p}{V_b} = 1 - \frac{V_s}{V_b}$, Eq.

(3.7) can be further simplified into

$$\nabla \cdot \mathbf{V}^s = \frac{1}{V_b} \frac{DV_b}{Dt}. \quad (3.8)$$

From the definition of the volume strain, we know that

$$\epsilon_v = \frac{DV_b}{V_b}. \quad (3.9)$$

After substitution of Eq. (3.9) into Eq. (3.8), we get

$$\nabla \cdot \mathbf{V}^s = \frac{D\epsilon_v}{Dt}. \quad (3.10)$$

In Eq. (3.10), the divergence of the solid phase velocity only reflects rates of bulk volume changes. Next we substitute Eq. (3.10) into the fluid flow Eq. (3.6) and get

$$\frac{D(\rho_f \phi)}{Dt} + \rho_f \phi \frac{D\epsilon_v}{Dt} = -\nabla \cdot (\rho_f \mathbf{V}^D). \quad (3.11)$$

We add and subtract the term $\epsilon_v \frac{D\rho_f \phi}{Dt}$ into Eq. (3.11):

$$\frac{D(\rho_f \phi)}{Dt} + \rho_f \phi \frac{D\epsilon_v}{Dt} + \epsilon_v \frac{D\rho_f \phi}{Dt} - \epsilon_v \frac{D\rho_f \phi}{Dt} = -\nabla \cdot (\rho_f \mathbf{V}^D), \quad (3.12)$$

then the second and third term in the left hand side can be combined into one term,

$$\frac{D(\rho_f \phi)}{Dt} + \frac{D\rho_f \phi \epsilon_v}{Dt} - \epsilon_v \frac{D\rho_f \phi}{Dt} = -\nabla \cdot (\rho_f \mathbf{V}^D). \quad (3.13)$$

Now we recall the assumption that the deformation is infinitesimal, which means ϵ_v is very small. Therefore, the third term on the left hand side $\epsilon_v \frac{D\rho_f \phi}{Dt}$ is much smaller compared to the first term and can be neglected. Thus Eq. (3.13) is

$$\frac{D\rho_f \phi(1+\epsilon_v)}{Dt} = -\nabla \cdot (\rho_f \mathbf{V}^D). \quad (3.14)$$

We usually define $\phi^* = \phi(1 + \epsilon_v)$ as the fluid traction or the Lagrangian porosity. Because of the infinitesimal deformation, the Lagrangian description and Eulerian description are equal. Therefore, $\partial(\cdot)/\partial t \approx D(\cdot)/Dt$. Finally, the governing equation considering geomechanics effects for the fluid flow (no source/sink term) is

$$\frac{\partial \rho_f \phi^*}{\partial t} = -\nabla \cdot (\rho_f \mathbf{V}^D). \quad (3.15)$$

In the section 3.5, we will extend the equation of the single phase flow to the two phase flow.

3.2 EDFM Model

Lee et al. (2001), Li and Lee (2008), Hajibeygi et al. (2011) and Moinfar et al. (2012) developed and improved the embedded discrete fracture model. EDFM applies the concept of wellbore index (WI) to derive a transport index between fracture and matrix cells. Moinfar et al. (2013) show that EDFM provides adequate accuracy for multiphase compositional simulation.

Because the fractures and matrices are modeled on different computational domains, there is no fluid communication between them in the mass balance equations. Consequently, we define non-neighboring connections (NNC) for EDFM. That is, each gridblock in the numerical model can communicate with any other gridblock through a non-neighboring connection.

The embedded fractures are discretized vertically and horizontally by the cell boundaries of gridblocks that are intersected by a fracture. Connection transmissibility is then introduced to account for the flux interaction between the fracture and the matrix. Li and Lee (2008) assume that the pressure around fracture is linearly distributed, and with this approximation, the average normal distance from the fracture in the gridblock is

$$\langle d \rangle = \frac{\int \mathbf{n} \cdot \mathbf{x} dS}{S}, \quad (3.16)$$

where \mathbf{n} is the unit normal vector; \mathbf{x} is the distance from the fracture; dS and S are the area element and area of the gridblock, respectively. Subsequently, the transmissibility is

$$T = \frac{kA}{\langle d \rangle}, \quad (3.17)$$

where A is the fracture surface area in the gridblock, and k is the harmonic average of the permeability of the hydraulic fracture and the matrix. For fractures that do not fully

penetrate a gridblock, it is assumed that T is linearly proportional to the fracture length inside the gridblock; therefore, the transfer term between a matrix cell and a segment of a fracture embedded in that cell is

$$q_{mf} = T(\psi_m - \psi_f), \quad (3.18)$$

where q_{mf} is the volumetric rate between the matrix gridblock and the fracture segment, T is the transmissibility between them, ψ_m and ψ_f are the matrix and fracture gridblock potential, respectively.

For a NNC between intersecting fracture cells, we use the same approach presented by Karimi-Fard et al. (2004), wherein the transmissibility is

$$T_{ff} = \frac{T_1 T_2}{T_1 + T_2}, \quad (3.19)$$

$$T_1 = \frac{k_{f1} \omega_{f1} L_{int}}{d_{f1}}, \quad T_2 = \frac{k_{f2} \omega_{f2} L_{int}}{d_{f2}}, \quad (3.20)$$

where L_{int} is the length of the intersection line bounded in a gridblock, ω_f is the fracture aperture and k_f is the fracture permeability. Likewise, d_f is the average of normal distances from the center of the fracture subsegments (located in each side of the intersection line) to the intersection line.

Such a NNC is required for any pair of intersecting fractures. Thus, if more than two fractures intersect in a gridblock, a NNC is defined between each pair of intersecting fracture control volumes. Also, if two fractures penetrating a gridblock do not intersect with each other within the gridblock, no NNC is needed.

For a NNC between two cells of an individual fracture, k is equal to the fracture permeability and d is the distance between the centers of two fracture segments. Parameter A is the fracture aperture times the length of this intersection line.

Before a fluid flow simulation, a list of NNC pairs, the arrangement of fracture cells, the arrangement of fracture cells, the transmissibility of NNCs, and the transmissibility between fracture cells should be computed on the basis of the grid structure and fracture planes. A preprocessing code is developed to provide the required data for flow simulations.

While EDFM facilitates the modeling of irregular fracture geometry, it is not very appropriate for unconventional reservoir modeling for the reason that it assumes a linear pressure variation in the normal direction to each fracture. The extreme contrast in conductivity between fractures and the ultra-tight matrix results in steep potential gradients that are difficult for EDFM to capture.

3.3 Dual Continuum Model

Dual-continuum models, widely used in the industry, are the conventional method for simulating natural fracture reservoirs (NFRs). Warren and Root (1963) introduced the dual porosity model to petroleum literature. The dual porosity model, which is also known as a sugar cube model, was first used for modeling single-phase flow in NFRs. In this model, rectilinear prisms of rock matrix are separated by an orthorhombic continuum of fractures. Dual porosity simulation involves discretization of the reservoir into two domains, matrix and fracture. Hence, every point in the reservoir contains fracture and matrix pressures and saturations. A dual porosity model presumes that the flow occurs from the matrix to the fractures, and then to the production wells. The rock matrix is where the majority of oil is stored. In the dual porosity model, matrix and fracture domains are linked to each other through an exchange term that connects each fracture cell to its corresponding

matrix cell in a gridblock. The matrix-fracture exchange rate is controlled by a shape factor. Also, the matrix blocks in the dual porosity approach are assumed to be isotropic and homogeneous. Figure. 3.1 shows an idealized sugar cube representation of a fractured reservoir, wherein highly interconnected orthogonal fractures are fed by numerous matrix blocks.

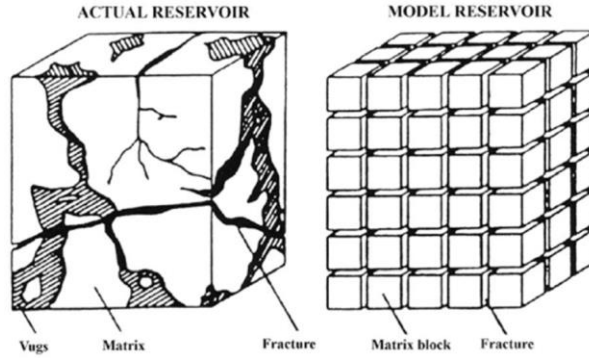


Figure 3.1 An idealized sugar cube of a fractured reservoir (Warren and Root 1963)

Considering a single-phase fluid flow, the mass conservation equations for the fracture and matrix domains in the dual porosity approach can be expressed for the fracture domain as

$$\frac{k_{fx}}{\mu} \frac{\partial^2 P_f}{\partial x^2} + \frac{k_{fy}}{\mu} \frac{\partial^2 P_f}{\partial y^2} + \frac{k_{fz}}{\mu} \frac{\partial^2 P_f}{\partial z^2} - q_{mf} = \phi_f C_f \frac{\partial P_f}{\partial t} \quad (3.21)$$

and for the matrix domain, as

$$\phi_m C_m \frac{\partial P_m}{\partial t} = q_{mf}, \quad (3.22)$$

The matrix-fracture transfer is represented by the pseudo-steady state relation:

$$q_{mf} = \frac{\sigma k_m}{\mu} (P_m - P_f), \quad (3.23)$$

where k is permeability, P is pressure, μ is fluid viscosity, C is total compressibility, ϕ is porosity, σ is shape factor, and q_{mf} is matrix-fracture flow rate per unit bulk volume. The

subscripts m and f refer to the properties in the matrix and fracture domains. The shape factor, which has the dimension of reciprocal area, reflects the geometry of matrix blocks and controls the interporosity flow between matrix and fracture domains.

3.3.1 Shape Factor

The matrix-fracture exchange is a critical component of any model that is used for the simulation of NFRs. In the Warren and Root approach, the matrix-fracture fluid transfer is assumed to take place under pseudo-steady state conditions. The matrix-fracture transfer function is proportional to a geometrical shape factor σ , and the driving force is the pressure difference between a matrix block and its surrounding fracture. Determination of the shape factor is not a simple task because of the potential for complex interaction between fractures and matrix rock of various shapes.

Originally, Warren and Root (1963) defined the shape factor as a parameter that depends on the geometry of matrix blocks:

$$\sigma = \frac{4n(n+2)}{L^2}, \quad (3.24)$$

where n is the number of normal sets of fractures ($n = 1, 2, 3$), and the characteristic length of matrix blocks is defined as

$$\begin{aligned} L &= a & n &= 1, \\ L &= \frac{2ab}{a+b} & n &= 2, \end{aligned}$$

or

$$L = \frac{3abc}{ab + ac + bc} \quad n = 3, \quad (3.25)$$

where a , b , and c are the lengths of the blocks faces.

Kazemi et al. (1976) used a finite-difference formulation for the flow between matrix and fractures and showed that for a three-dimensional case:

$$\sigma = 4 \left(\frac{1}{L_x^2} + \frac{1}{L_y^2} + \frac{1}{L_z^2} \right), \quad (3.26)$$

where L_x , L_y , and L_z are the distances between fractures in the x , y , and z directions, respectively.

These shape factors assume that the pseudo-steady state assumption is valid. Lim and Aziz (1995) considered the physics of pressure diffusion from the matrix to the fracture and presented an alternate shape factor:

$$\sigma = \pi^2 \left(\frac{1}{L_x^2} + \frac{1}{L_y^2} + \frac{1}{L_z^2} \right). \quad (3.27)$$

They performed simulations to investigate the accuracy of various shape factors using fine-grid simulations. The results showed that their shape factor in Eq. (3.27) matches results of the fine-grid single porosity better, indicating that the pseudo-steady state assumption is not a suitable one and that the pressure gradients in the matrix should be taken into account in the calculation of shape factors. They also showed that the dual porosity simulation using the Warren and Root's shape factor overestimates the recovery, while the simulation using the Kazemi's shape factor underestimates the recovery.

3.4 Geomechanical Effects on Porosity and Permeability

3.4.1 Geomechanical Effects on the Properties of Dual Continua

We assume that natural fractures consist of a continuum that has a well-defined concept of porosity. Porosity is a function of a volume strain and a fluid pressure. Thus the same type of equation for the porosity update can apply to both the matrix and fracture continuum. Gai et al. (2003) provides the relationship between the porosity, fluid pressure, and the volumetric strain under infinitesimal deformations as

$$\phi^* = \phi^0 + \alpha \epsilon_v + \frac{1}{M} p, \quad (3.28)$$

where ϕ^0 is the initial porosity in each continuum, α and M^{-1} are the Biot's coefficient and Biot's poroelastic parameter for the matrix or the natural fracture continuum, respectively, p is the matrix pressure.

In unconventional reservoirs, the matrix permeability is rather small ($10^{-17} \sim 10^{-20} \text{ m}^2$). Therefore, the change of matrix permeability has less effect on the flow compared to that of natural and hydraulic fractures. We assume that the matrix permeability is constant.

Permeability in natural fractures is mainly affected by the aperture. According to the cubic law, the permeability of a cracked system (Izadi, 2011) is

$$\frac{k}{k_0} = \left(1 + \frac{\Delta b}{b_0}\right)^3, \quad (3.29)$$

where Δb is the aperture change in natural fractures, which is a function of the strain and b_0 is the initial natural fracture aperture.

The assumption that the aperture change is a function of a strain has been supported by previous research (Liu, 2010). We calculate the average fracture aperture change Δb in the x and the y directions for each grid block. In Figure. 3.2, S is the spacing of natural fractures, b is the natural fracture aperture, and the solid line boundary and dashed line boundary represent the configuration before and after deformation

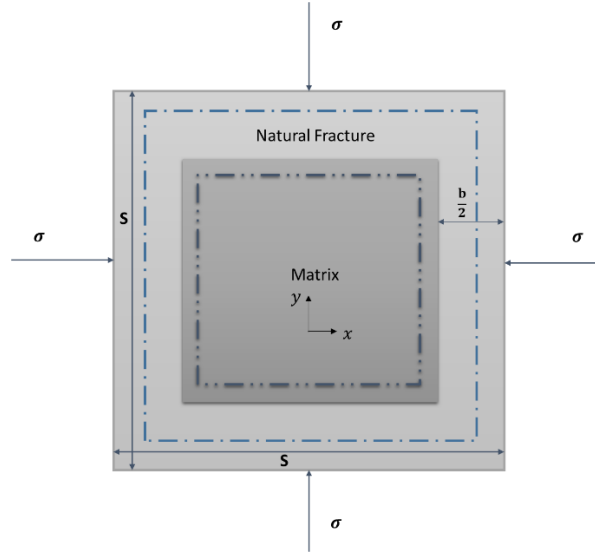


Figure 3.2 Schematic of fracture aperture change due to strain.

We can derive the relationship between the average aperture and strain changes due to external forces. From the definition, we write out the total and matrix volumetric strains, individually as

$$\epsilon = \frac{\Delta x}{S} + \frac{\Delta y}{S} \quad (3.30)$$

and

$$\epsilon_m = \frac{\Delta x - \Delta b}{S} + \frac{\Delta y - \Delta b}{S}, \quad (3.31)$$

where Δx and Δy are length changes in the x and the y directions.

Substituting Eqs. (3.30) and (3.31) into $\epsilon = \epsilon_m + \epsilon_f$, we get

$$\Delta b = \frac{S\epsilon_f}{2}. \quad (3.32)$$

For the scenario that each dual porosity grid block is cut by a hydraulic fracture, there is a discontinuity of strain across the hydraulic fracture. We calculate strains in two regions that are separated by the hydraulic fracture and take the average value ϵ_f from each part.

3.4.2 Geomechanical Effects on Hydraulic Fracture Permeability

We treat the hydraulic fracture as a void space and consider permeability as a function of a fracture aperture. According to the Poiseuille law, the fracture permeability is proportional to the square of the fracture aperture (Moinfar et al., 2013):

$$k_f = k_f^0 \left(\frac{\omega_f}{\omega_f^0} \right)^2. \quad (3.33)$$

3.5 Discretization

In the flow simulation, we use a fully implicit, first order backward Euler scheme in time and a finite volume method in space. In the following equations, the subscript $\alpha \in \{g, w\}$ denotes either gas or water phases. Subscripts m, f, F represent the matrix, the natural fracture and the hydraulic fracture respectively. Superscript n denotes the time step.

For the matrix cell i , we only consider the fluid flow between the matrix and the surrounding natural fracture continuum. The discretized form is

$$\begin{aligned} & (V_i S_{\alpha,i} \rho_{\alpha,i} \phi_{m,i}^*)^{n+1} - (V_i S_{\alpha,i} \rho_{\alpha,i} \phi_{m,i}^*)^n \\ & - \Delta t \left(T_{\alpha,mf,ii} \frac{k_{r\alpha}}{\mu_\alpha} \rho_\alpha \Delta \Phi_{\alpha,mf,ii} \right)^{n+1} = 0, \end{aligned} \quad (3.34)$$

where V_i is the volume of the grid block i , $\phi_{m,i}^*$ is the fluid fraction of matrix i , $T_{\alpha,mf,ii}$ is the transmissibility between matrix i and natural fractures i , Δt is the time step, $\Delta\Phi_{\alpha,mf,i}$ is the potential difference of the matrix i and the natural fracture i .

For the natural fracture continuum in the block i , There is the flow between the matrix and the fracture as well as flow between hydraulic fractures that intersect natural fractures.

$$\begin{aligned} & (V_i S_{\alpha,i} \rho_{\alpha,i} \phi_{f,i}^*)^{n+1} - (V_i S_{\alpha,i} \rho_{\alpha,i} \phi_{f,i}^*)^n \\ & + \Delta t \left(T_{\alpha,mf,ii} \frac{k_{r\alpha}}{\mu_\alpha} \rho_\alpha \Delta\Phi_{\alpha,mf,ii} \right)^{n+1} - \sum_{j=1}^{n_{faces}} \Delta t \left(T_{\alpha,ff,ij} \frac{k_{r\alpha}}{\mu_\alpha} \rho_\alpha \Delta\Phi_{\alpha,ff,ij} \right)^{n+1} - \\ & \sum_{j=1}^{n_{fF}} \Delta t \left(T_{\alpha,fF,ij} \frac{k_{r\alpha}}{\mu_\alpha} \rho_\alpha \Delta\Phi_{\alpha,fF,ij} \right)^{n+1} = 0, \end{aligned} \quad (3.35)$$

where $\phi_{f,i}^*$ is the fluid fraction of natural fracture continuum i , n_{faces} is the number of natural fractures j neighboring to the natural fracture continuum i , n_{fF} is the number of connections between the natural fracture i and the hydraulic fracture j , $T_{\alpha,ff,ij}$ is the transmissibility between the natural fractures i and j , $T_{\alpha,fF,ij}$ is the transmissibility between the natural fracture i and the hydraulic fracture j , $\Delta\Phi_{\alpha,ff,ij}$ is the potential difference of the natural fracture i and the natural fracture j , $\Delta\Phi_{\alpha,fF,ij}$ is the potential difference of the natural fracture i and the hydraulic fracture j .

For each hydraulic segment i , we assume that the fluid flow occurs between the hydraulic segment and its neighboring hydraulic segment as well as between the hydraulic segment and the natural fractures.

$$(V_i S_{\alpha,i} \rho_{\alpha,i} \phi_{F,i})^{n+1} - (V_i S_{\alpha,i} \rho_{\alpha,i} \phi_{F,i})^n + \sum_{j=1}^{n_{FF}} \Delta t \left(T_{\alpha,FF,ij} \frac{k_{r\alpha}}{\mu_\alpha} \rho_\alpha \Delta\Phi_{\alpha,FF,ij} \right)^{n+1} +$$

$$\Delta t \left(T_{\alpha, fF, ij} \frac{k_{r\alpha}}{\mu_{\alpha}} \rho_{\alpha} \Delta \Phi_{\alpha, fF, ij} \right)^{n+1} = 0, \quad (3.36)$$

where $\phi_{F,i}$ is the porosity of the hydraulic fracture which is constant in this thesis, $T_{\alpha, FF, ij}$ is the transmissibility between the hydraulic segments i and j , $\Delta \Phi_{\alpha, FF, ij}$ is the potential difference of the hydraulic segments i and j .

3.6 Solution Algorithm

Coupling methods between the reservoir flow and the solid deformation can be classified into three different types: iteratively coupled, fully coupled, and explicitly coupled (Tran and Settari, 2004). These three coupling methods are reviewed next.

1. Iteratively coupled: This approach solves flow and geomechanics variables iteratively within a time step until a desired accuracy is reached. For the coupled geomechanics and flow, there are two schemes: drained-split and undrained-split. In the drained-split scheme, pore pressure is frozen during the mechanical solve. In the undrained-split scheme, when mechanics deformation is being calculated, fluid mass content is fixed, and fluid is not allowed to flow. Iteratively coupled methods feature flexibility and modularity because different linear solvers could be designed according to the structure of the matrix in each sub problem; but sometimes an iteratively coupled method could cause numerical instability. This is particularly true when rock tends to increase in volume with a reduction in pore pressure (e.g., owing to dilation during shearing) (Gutierrez et al., 2001).

2. Fully coupled: This approach solves flow variables, such as pressure, saturation, temperature, and geomechanical responses at once using Newton's method. The fully coupled system has unconditional stability. Compared to the iteratively coupled method, it solves a larger augmented Jacobian matrix at every Newton iteration.

3. Explicitly coupled: this method is sometimes referred as one-way coupling. In this coupling, information is only transferred from a flow simulator to a geomechanics simulator. Here, changes in the fluid pressure affect changes in the stress and strain field,

and the stress and strain field changes do not affect the fluid pressure (Tran and Settari, 2004).

In this study, we use a mixed-space discretization. A finite volume method is applied to fluid flow in which the pressure is at the center of the grid block. XFEM is used for poromechanics where the displacement vector is located at vertices.

The final linear system for the coupled geomechanics and flow is a compact 3×3 matrix:

$$\begin{pmatrix} A_{pp} & C_{ps} & C_{pu} \\ C_{sp} & A_{ss} & C_{su} \\ C_{up} & C_{us} & K_{uu} \end{pmatrix} \begin{pmatrix} p \\ s \\ u \end{pmatrix} = \begin{pmatrix} F_p \\ F_s \\ F_u \end{pmatrix}, \quad (3.37)$$

where p is the pressure vector, s is the saturation vector, and u is the displacement vector.

In the 3×3 matrix, each term is a coupling coefficient sub matrix between different items (p, s, u) . We solve the coupled system using the fully coupled method.

CHAPTER 4

NUMERICAL CASES

4.1 Mandel's Problem

Abousleiman et al. (1996) presented a canonical example of nonmonotonic behavior in pore pressure following undrained loading. In Figure. 4.1, a rectangular plate of length $2a$ and width $2b$ is sandwiched between two rigid, impermeable plates. A compressive force F is applied and is held constant. F is the force per unit length in the z direction. The fluid pressure is constant at the left and right boundaries. Because of the symmetry in the domain, only one quarter of the plate is analyzed.

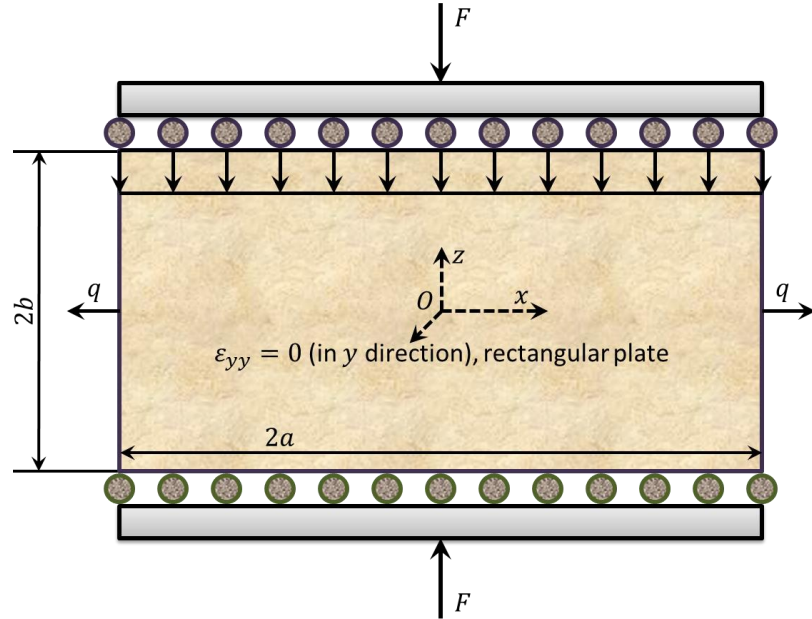


Figure 4.1 Illustration of Mandel's problem

The analytical solution for pore pressure is (Abousleiman et al., 1996)

$$p = \frac{2FB(1+v_u)}{3a} \sum_{i=1}^{\infty} \frac{\sin \beta_i}{\beta_i - \sin \beta_i \cos \beta_i} \left(\cos \frac{\beta_i x}{a} - \cos \beta_i \right) \exp \left(-\frac{\beta_i^2 ct}{a^2} \right), \quad (4.1)$$

where

$$\tan \beta_i = \frac{(1-v)}{v_u - v} \beta_i, \quad (4.2)$$

and the Skempton pore pressure coefficient B , undrained Poisson's ratio v_u and diffusivity coefficient c (Rice, 1976) are

$$B = 1 - \frac{\phi K(K_s - K_f)}{K_f(K_s - K) + \phi K(K_s - K_f)}, \quad (4.3)$$

$$v_u = \frac{3v + B(1-2v)\left(1 - \frac{K}{K_s}\right)}{3 - B(1-2v)\left(1 - \frac{K}{K_s}\right)}, \quad (4.4)$$

and

$$c = \frac{2kB^2G(1-v)(1+v_u)^2}{9\mu_f(1-v_u)(v_u-v)}, \quad (4.5)$$

where K, K_s, K_f are the bulk moduli of the porous media, solid grains and fluid respectively, and v is the drained Poisson's ratio.

Table 4.1 gives the dimension of the specimen and material properties used in the simulation. Figure. 4.2 shows the pressure distribution along the x axis with time. The pressure in the plate interior first builds up at early time before the entire domain starts to deplete. The numerical solution gives results in agreement with the analytical solution.

Table 4.1 Input parameter for Mandel's problem

Input Data	Value	Unit
Grid Size	$50 \times 50 \times 1$	
Plate Size	$200 \times 2 \times 1$	m \times m
Porosity	0.2	
Permeability	10^{-13}	m ²
Young's modulus	10^8	Pa
Drained Poisson's ratio	0.2	
Undrained Poisson's ratio	0.4	
Biot's coefficient	1.0	
Overburden F	10^6	Pa

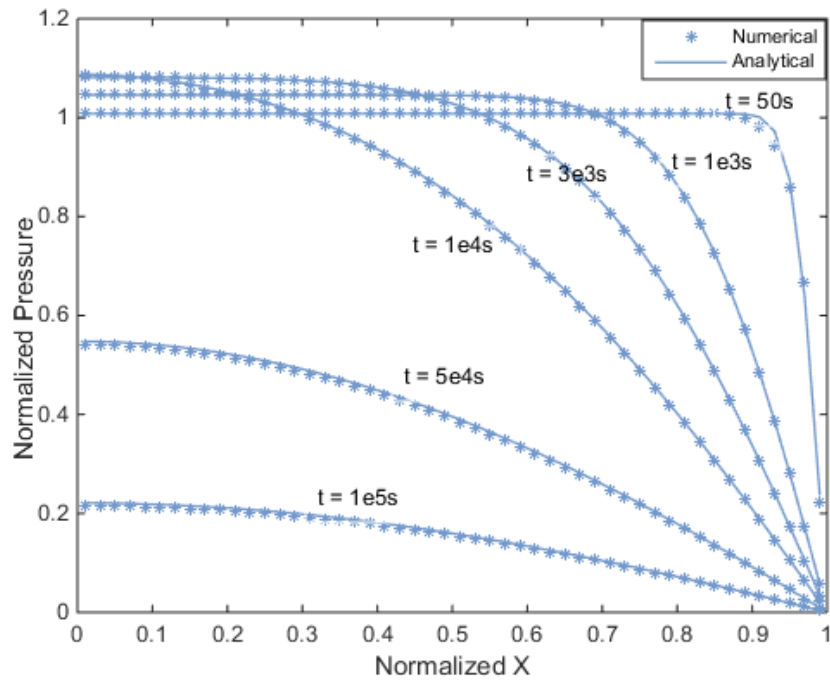


Figure 4.2 Mandel's problem validation

4.2 Single Fracture Mechanics

Stress intensity factor (SIF) is an important parameter for linear elastic fracture mechanics and for the assessment of the performance of XFEM (Khoei, 2014). The normalized stress intensity factor is $\overline{K_I} = \frac{K_I}{\sigma\sqrt{\pi a}}$.

First, we validate our XFEM implementation using an infinite plate with a center crack in the domain in Figure. 4.3. The exact elasticity solution is used as an input, imposing the displacement field on the boundaries of a finite plate. Only the right half of the plate is modeled due to symmetry. Four different finite element meshes of dimensions 5×10 , 10×20 , 20×40 and 40×80 are compared. The input parameters are $\sigma_\infty = 10^6 \text{Pa}$, $E = 10^8 \text{Pa}$, Half Area = $10 \times 20 \text{ m}^2$, crack half-length $a = 5.35 \text{ m}$ and a plane stress condition.

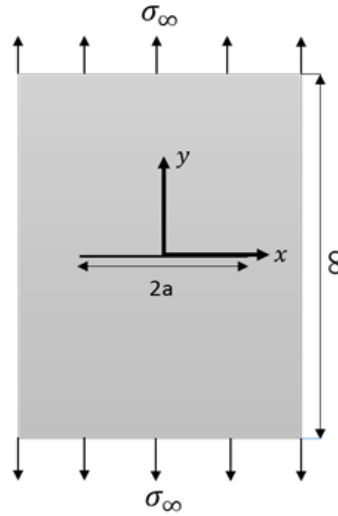


Figure 4.3 Schematic of a center crack in a infinite plane

The analytical solution for the crack opening displacement under a plane stress condition (Janssen et al., 2006) is

$$w = \frac{2\sigma_\infty}{E} \sqrt{a^2 - x^2} \quad (4.6)$$

Figure 4.4 shows a comparison of our numerical results for the crack opening displacement (mesh 40×80) to the analytical solution, A satisfactory agreement is observed.

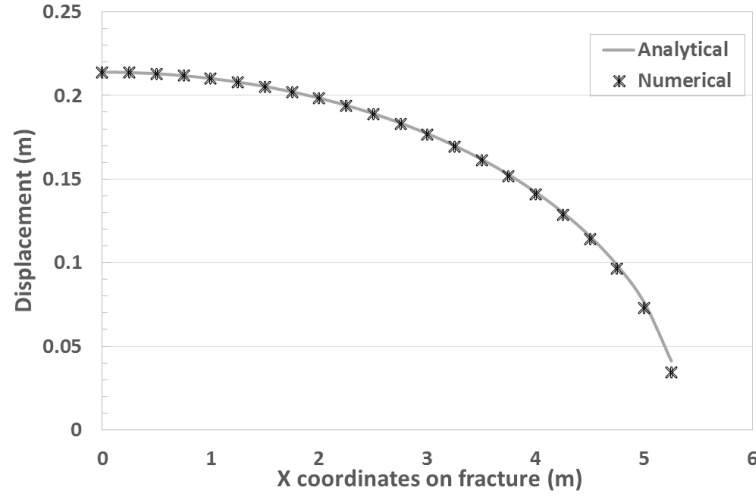


Figure 4.4 Crack opening displacement versus X coordinates on fracture

The numerical calculation of the J integral is to evaluate the interaction integral $I^{(1,2)}$ (Moës et al., 1999)

$$I^{(1,2)} = \int_A \left[\sigma_{ij}^{(1)} \frac{\partial u_i^{(2)}}{\partial x_1} + \sigma_{ij}^{(2)} \frac{\partial u_i^{(1)}}{\partial x_1} - \sigma_{ij}^{(1)} \varepsilon_{ij}^{(2)} \delta_{1j} \right] \frac{\partial q}{\partial x_j} dA, \quad (4.7)$$

where A is the integral domain which is shown in dark grids in Figure. 4.5, A is the grid blocks that are cut by the dashed circle, $\sigma_{ij}^{(1)}, u_i^{(1)}$ are the numerical solutions of the stress and displacement near the tip, $\sigma_{ij}^{(2)}, u_i^{(2)}$ are the analytical solutions near the tip which are listed in the Chapter 2, δ_{ij} is the Kronecker delta, $q(x)$ is the smoothing weighting

function which takes a value of unity on an open set containing the crack tip and vanishes on an outer prescribed dashed circle.

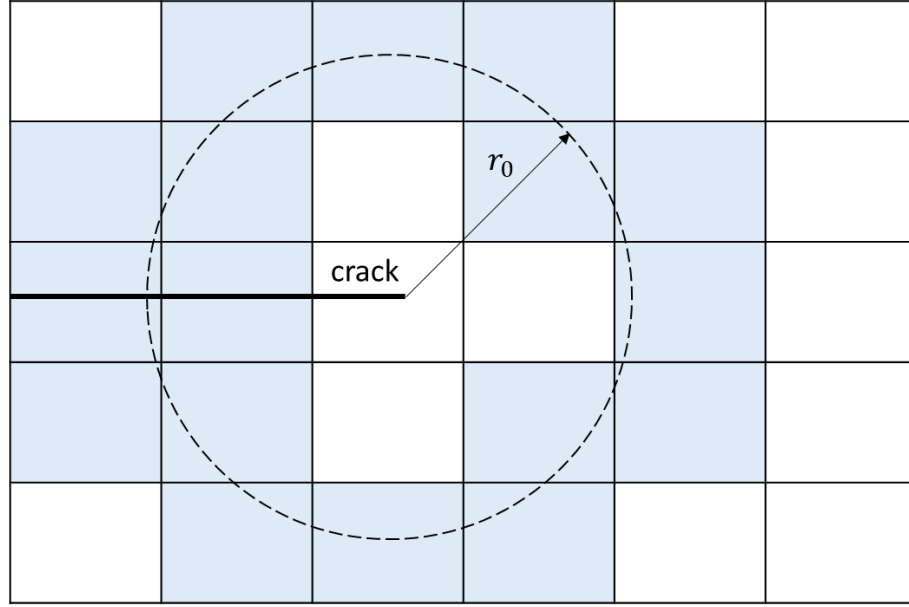


Figure 4.5 Element selected (dark grids) near the crack tip for the J integral

After we calculate the J integral, the stress intensity factor K can be calculated by

$$K = \frac{2}{E'} I^{(1,2)}, \quad (4.8)$$

where E' is equal to E under the plane stress condition and equal to $\frac{E}{1-\nu^2}$ under the plane strain condition.

The analytical solution for this problem is $\overline{K_I} = 1$ (Huang et al. 2003). In Table 4.2, we perform the J-Integral near the crack tip and calculate the numerical result, $\overline{K_I}$, which reaches excellent accuracy.

Table 4.2 Normalized values of the stress intensity factors

Number of Nodes	Normalized $\overline{K_I}$	Error %
66	1.01449	1.4
231	1.00861	0.86
861	1.0047	0.47
3321	1.0024	0.24

Next, we rotate the fracture β degrees from its center counterclockwise. The analytical solution for the normalized stress intensity factor has been known as $\overline{K_I} = \cos^2 \beta$.

Figure. 4.6 shows the comparison of the stress intensity factor K_I obtained by analytical and numerical methods. A good agreement is reached between numerical and analytical results.

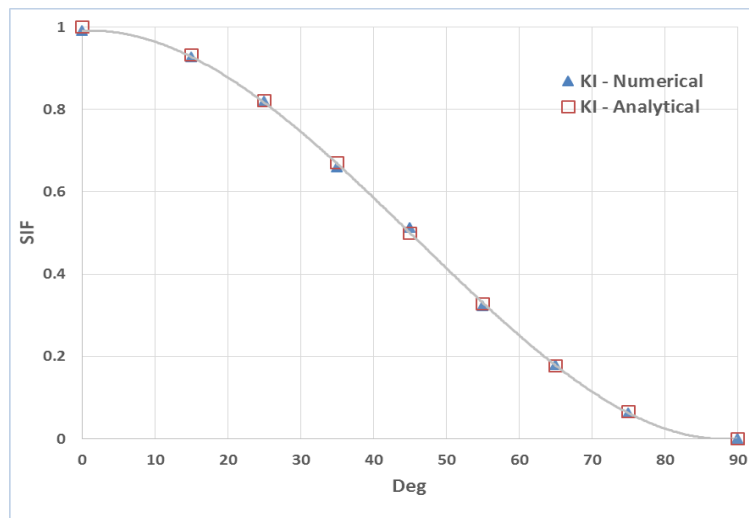


Figure 4.6 Inclined crack stress intensity factor

4.3 Convergence Analysis

We perform a grid refinement study of the XFEM-EDFM simulator without considering dual porosity. Figure. 4.7 depicts the fractured domain. The boundary of the reservoir is impermeable to the fluid flow. On the top and right sides of the reservoir, two constant forces are exerted. On the left and bottom sides, displacements are prescribed as zero. Five different numbers of grid blocks (25×25 , 50×50 , 100×100 , 200×200 , 400×400) are created for the displacement. Another five different numbers of grid blocks (5×5 , 15×15 , 45×45 , 135×135 , 405×405) are created for the pressure. The input parameters are listed in Table 4.3.

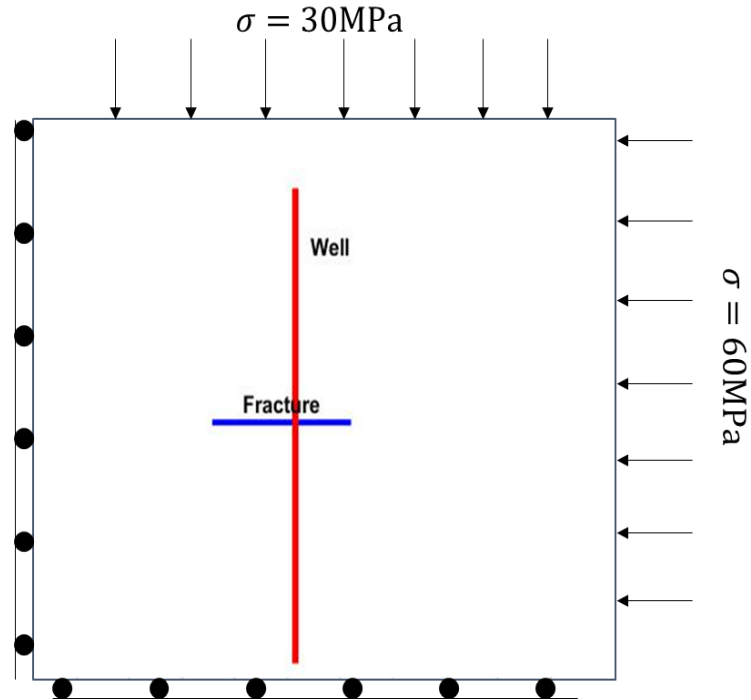


Figure 4.7 A schematic of a single hydraulic fracture in the unconventional reservoir

Table 4.3 Parameters for grid refinement.

Input Data	Description	Value	Unit
$L_x \times L_y$	reservoir size	200×200	$\text{m} \times \text{m}$
D_i	fracture width	0.005	m
x_f	fracture length	51	m
ϕ	matrix porosity	0.2	
k_m	matrix permeability	10^{-18}	m^2
k_{Fi}	hydraulic fracture permeability	10^{-12}	m^2
E_m	matrix Young's modulus	50	GPa
ν_m	matrix Poisson's ratio	0.2	
α_m	matrix Biot's coefficient	0.8	
E_p	proppant Young's modulus	500	MPa
p_i	reservoir initial pressure	20	MPa
S_w	water saturation	0.4	
p_w	well pressure.	5	MPa

The coarsest mesh (400×400 for displacement, 405×405 for pressure) in each test is chosen as the reference solution. The remaining mesh sizes are compared to the reference, and L2-norm is calculated. The error is defined as

$$\varepsilon = \frac{\sqrt{\sum_{i=1}^n (x_i - x_{\text{ref}})^2}}{\sqrt{\sum_{i=1}^n x_{\text{ref}}^2}}. \quad (4.9)$$

The grid refinement result for pressure and displacement appear on Figure. 4.8 and Figure. 4.9. From the plots, we find that error level of displacement is much smaller than pressure.

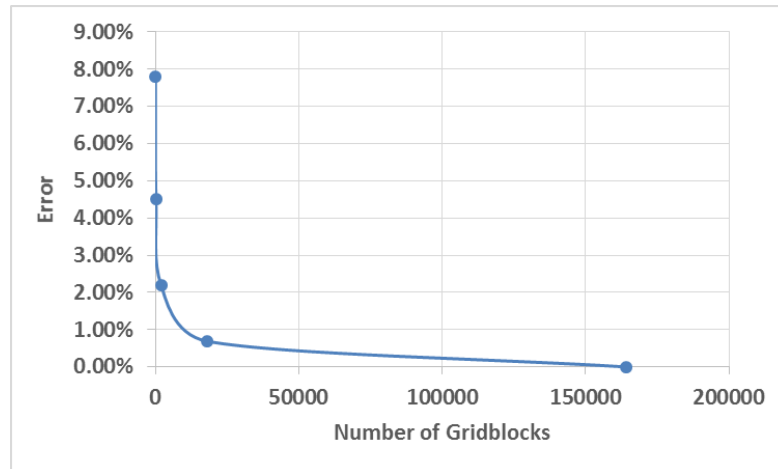


Figure 4.8 Error in pressure versus number of grid blocks

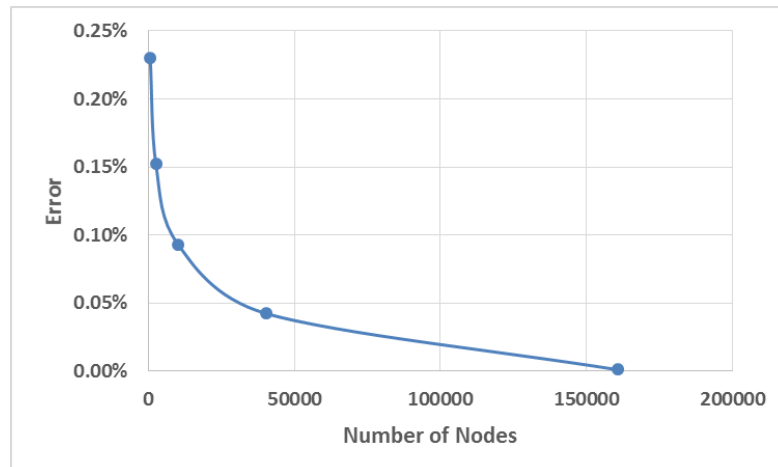


Figure 4.9 Error in displacement versus number of nodes

4.4 Synthetic Field Examples

We introduce two cases to test the EDFM-XFEM with dual porosity. In the following simulations, hydraulic fractures are treated explicitly while natural fractures are assumed as orthogonal continua that surround the matrix.

4.4.1 Effects of Natural Fracture Properties on the Coupled System

We introduce a two-dimensional problem with multiple hydraulic fractures as well as the dual porosity property for each grid block in the domain as depicted in Figure. 4.10. The reservoir has a length scale of $200 \text{ m} \times 200 \text{ m}$. The domain has 100×100 grid blocks. There is one horizontal well that produces gas and water. The well is intersected by four hydraulic fractures with different lengths (from bottom to up, 82, 82, 42, and 56m). There is no flow through the reservoir boundaries. The displacement is fixed on the left and bottom sides of the boundary. Constant forces are applied to the upper and the right sides.

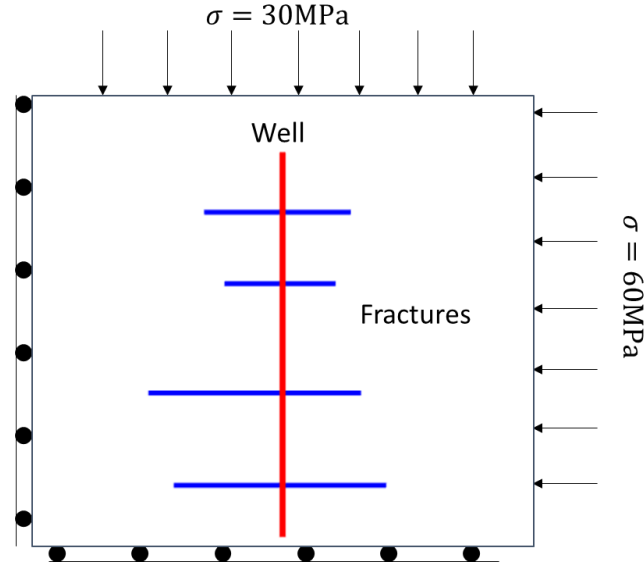


Figure 4.10 A schematic of a hydraulically fractured unconventional reservoir

For flow, the initial reservoir pressure is 20MPa, and the initial water saturation S_w is 0.4. The initial permeability and porosity of the fracture continuum are $k_{fi} = 10^{-13} \text{ m}^2$ and $\phi_f = 0.8$, whereas, the initial permeability and porosity of the matrix continuum are $k_m = 10^{-18} \text{ m}^2$ and $\phi_m = 0.1$. The initial aperture of natural fractures and hydraulic fractures are 0.001 m and 0.005 m respectively. The well pressure is kept constant at $p_w = 5 \text{ MPa}$.

For mechanics, the Young's modulus for the matrix grain is $E_m = 5 \text{ GPa}$, and the drained Poisson's ratio is $\nu = 0.2$. In this case, we study the influence of the natural fracture normal stiffness K_n on the natural fracture aperture and production rates. Three different values of the natural fracture normal stiffness K_n equal to 40, 60 and 100 $\text{GPa} \cdot \text{m}^{-1}$ are investigated. The shear stiffness of the natural fracture is fixed at $K_{sh} = 33 \text{ GPa} \cdot \text{m}^{-1}$.

m^{-1} . The Young's modulus of proppant is $E_p = 50 \text{ MPa}$. Biot's coefficients for matrix and natural fractures are $\alpha_m = 0.8$ and $\alpha_f = 0.9$. The plane strain condition is assumed.

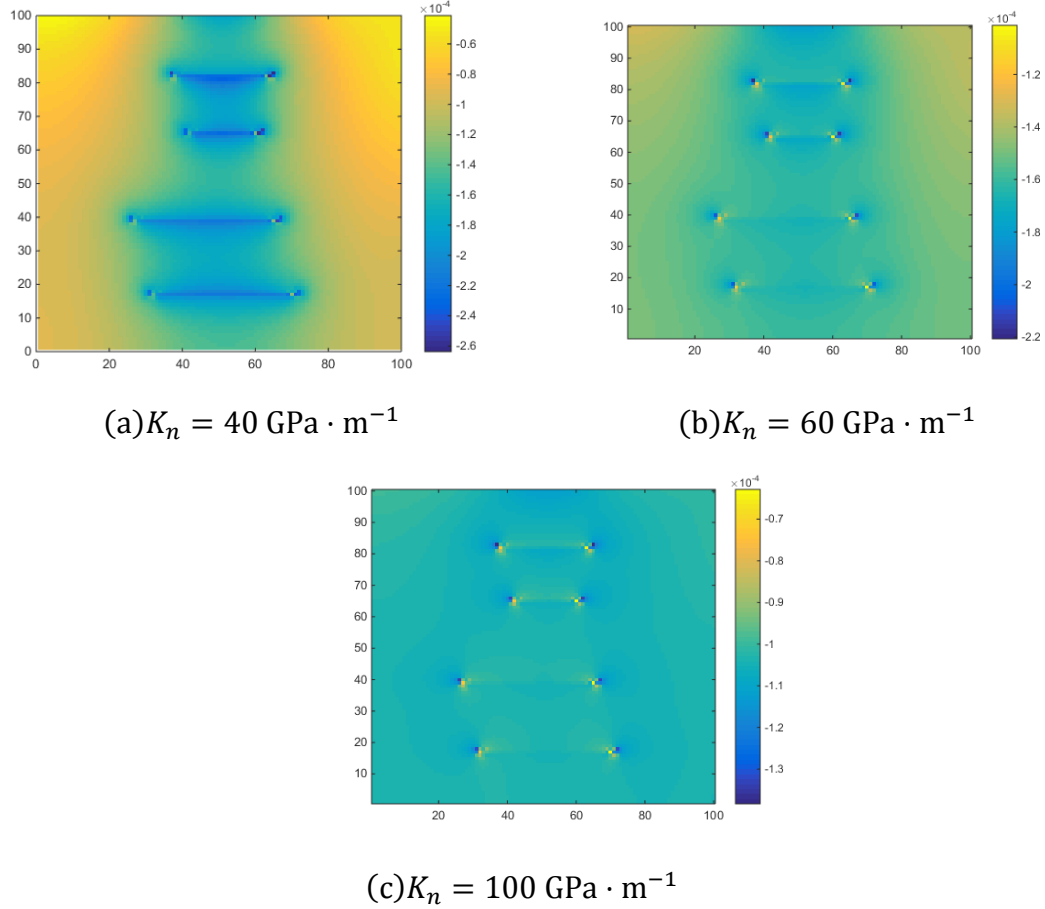


Figure 4.11 Natural fracture aperture changes at $t = 200$ days

The spacial profiles of natural fracture aperture changes appear in Figure 4.11. The natural fracture aperture change is determined both due to external forces and pore pressure. We find that when the natural fracture normal stiffness, K_n , increases, the fracture matrix system becomes stiffer as well. Accordingly, a smaller deformation of natural fracture occurs. It is also shown that natural fracture aperture changes at the tips are always larger than at other places. It is because the stress σ_{yy} at the tips tends to be singular for the linear fracture, which leads to a larger decrease in the natural fracture aperture. Another

interesting phenomenon is that there is an obvious contrast of aperture changes between places near the well and far away from the well at $K_n = 40 \text{ GPa} \cdot \text{m}^{-1}$. While K_n increases, the contrast diminishes. The smaller normal stiffness K_n leads to larger decreases in the natural fracture aperture. As a result, a lower permeability field forms and the pressure wave transmits slowly in the reservoir. Accordingly, pressure differences near the well and far away from the well are larger at $K_n = 40 \text{ GPa} \cdot \text{m}^{-1}$ than that at $K_n = 60, 100 \text{ GPa} \cdot \text{m}^{-1}$. Therefore, an apparent contrast is observed when K_n is equal to $40 \text{ GPa} \cdot \text{m}^{-1}$.

In Figure. 4.12, we plot gas production rates versus time for three different values of the normal stiffness. The larger normal stiffness K_n is, the smaller aperture changes. Therefore a higher permeability field will lead to higher production rates at early days. However, at around $t = 130$ days, production rates of $K_n = 60 \text{ GPa} \cdot \text{m}^{-1}$ and $K_n = 100 \text{ GPa} \cdot \text{m}^{-1}$ become almost the same.

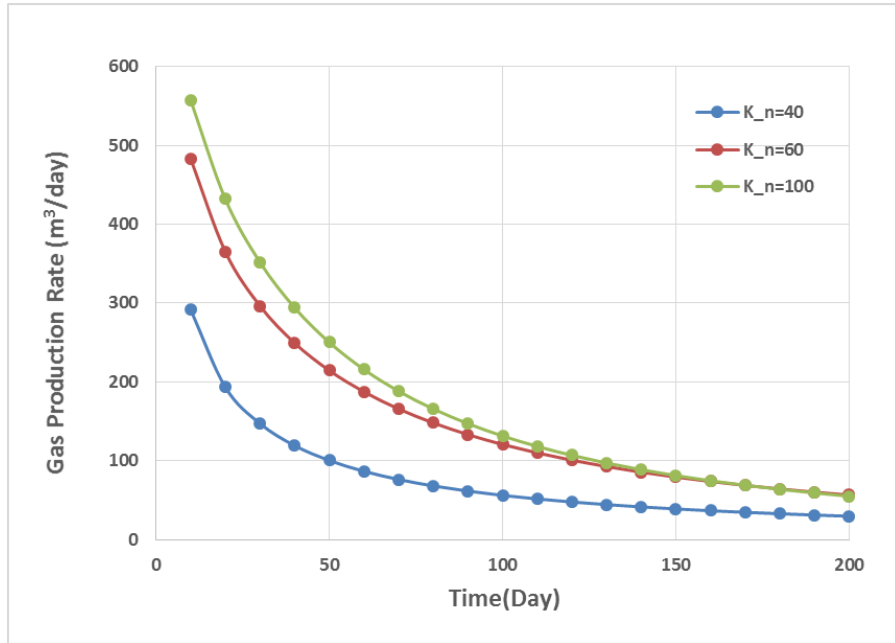


Figure 4.12 Gas production rate versus time

4.4.2 Effects of Proppant Properties on the Coupled System

Next, we vary the Young's modulus of proppant and observe the influence on the hydraulic fracture aperture and production rates. The hydraulic fracture pattern appears in Figure. 4.13.

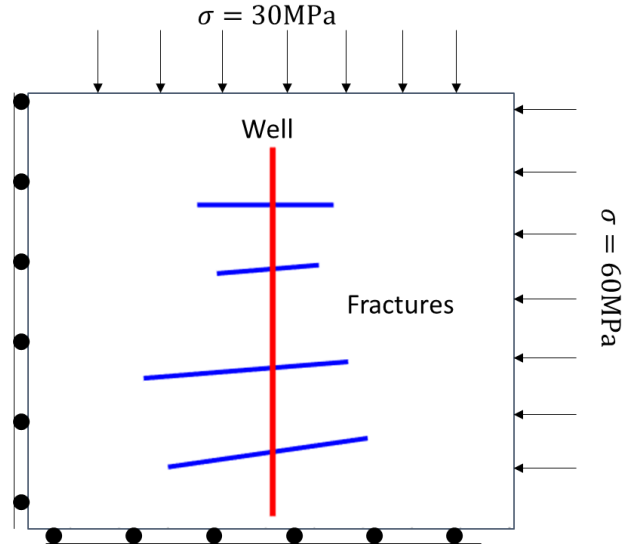


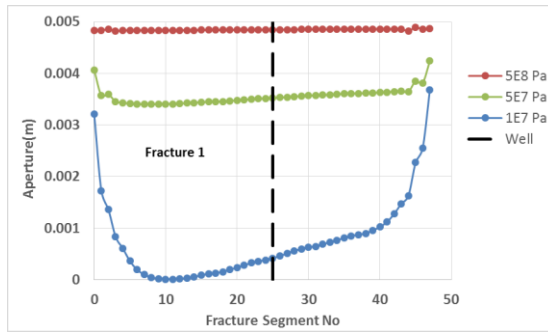
Figure 4.13 A schematic of a hydraulically fractured unconventional reservoir

In this scenario, we fix the normal stiffness at $K_n = 60 \text{ GPa} \cdot \text{m}^{-1}$. Three values of the proppant Young's modulus, E_p , are 10 MPa, 50 MPa and 500 MPa individually. The remaining parameter values are the same as the last case. The starting and ending points of fractures are listed in the Table 4.4.

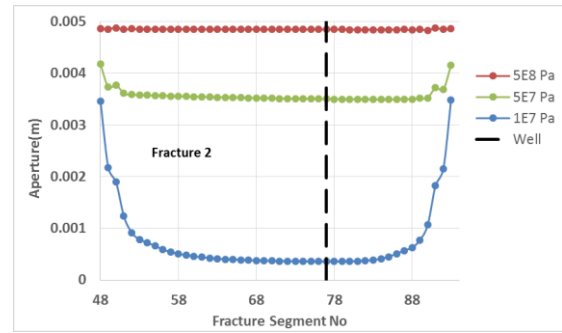
Table 4.4 Hydraulic fracture position information

Fracture No	Starting point	Ending point
1	(61, 33)	(141, 47)
2	(51, 77)	(133, 85)
3	(81, 129)	(121, 133)
4	(73, 163)	(127, 163)

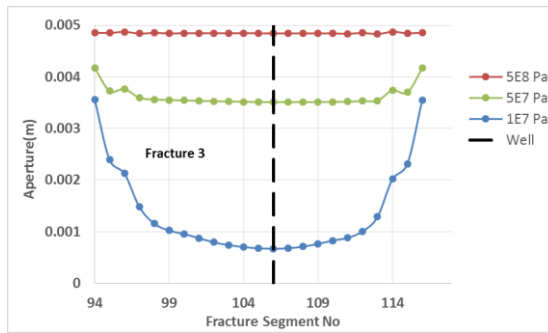
Each hydraulic fracture is intersected by several grid blocks and each intersected segment is called a fracture segment. In Figure. 4.14, the fracture number is ordered from the bottom to the top, and the fracture segment number is ordered from the left to the right and the bottom to the top. The black dashed line represents the well that intersects the hydraulic fracture. We observe that when the proppant is stiffer, the hydraulic fracture closes less. The fracture aperture almost does not change along the fracture plane when E_p is equal to $5E8$ Pa. In all cases, the aperture at the tips is always larger than at the center. It is because along the fracture plane, the region around tips is always stiffer than that at the center. The stiffer region is more able to stand compaction forces on the boundary and the reduction in the pore pressure.



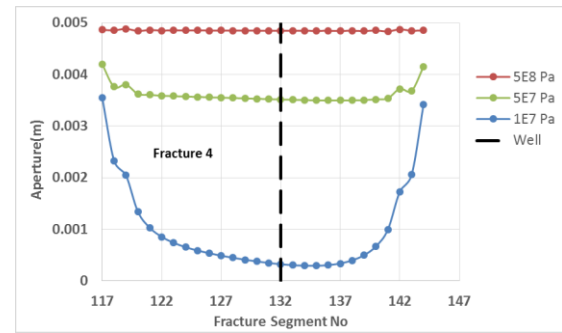
(a)



(b)



(c)



(d)

Figure 4.14 Hydraulic fracture aperture after production for 1000 days

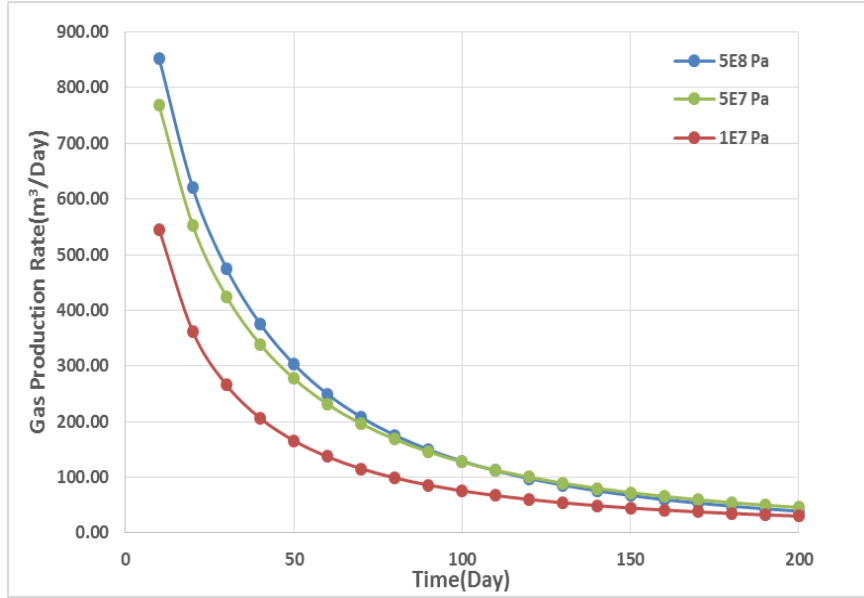


Figure 4.15 Gas production rate versus time

In Figure. 4.15, we compare the production rates for different values of the proppant Young's modulus over the first 200 days. As expected, the stiffest proppant gives the highest production rates. However, the production rate differences between $E_p = 5E8$ Pa and $5E7$ Pa are not very significant. After 200 days, the all three production rates tend to be the same.

CHAPTER 5

CONCLUSIONS

In this work, we develop a fully coupled flow and geomechanics simulator using the combined XFEM-EDFM and dual porosity model approach with a fully implicit time-stepping strategy. A novel proppant model is proposed to simulate production in hydraulically fractured reservoirs. The model is validated against available analytical solutions and mesh refinement studies are performed.

Using the proposed method, we first investigate the influence of natural fracture normal stiffness on the natural fracture aperture. It is confirmed that a lower normal stiffness causes larger deformation of natural fracture continua and consequently slows the pressure propagation in the reservoir.

Secondly, we study the proppant's impact on the hydraulic aperture and gas production rates. Results show that stiffer proppant could increase gas production rates. However, increasing the stiffness of the proppant may be only effective in improving production rates at the early time. After the production for a while, all of reservoirs with different proppant properties tend to have the same production rate.

We recommend to do the following to improve the simulator:

1. Use iterative solvers to solve the linear equation system.
2. Consider fracture contact phenomena in the simulator.
3. Consider hydraulic fracture propagation in the reservoir.
4. Extend the current framework to 3 dimensions.

BIBLIOGRAPHY

Abousleiman, Y., Cheng, A.D., Cui, L., Detournay, E. and Roegiers, J.C., 1996. Mandel's problem revisited. *Geotechnique*, 46(2), pp.187-195.

Azizi, N., Behbahani, R., Isazadeh, M.A., An Efficient Correlation for Calculating Compressibility Factor of Natural Gases, *Journal of Natural Gas Chemistry*. 19: 642-645, 2010.

Bai, M., 1999. On equivalence of dual-porosity poroelastic parameters. *Journal of Geophysical Research: Solid Earth*, 104(B5), pp.10461-10466.

Belytschko, T., Moës, N., Usui, S. and Parimi, C., 2001. Arbitrary discontinuities in finite elements. *International Journal for Numerical Methods in Engineering*, 50(4), pp.993-1013.

Berryman, J.G. and Wang, H.F., 1995. The elastic coefficients of double-porosity models for fluid transport in jointed rock. *JOURNAL OF GEOPHYSICAL RESEARCH-ALL SERIES-*, 100, pp.24-611.

Berryman, J.G., 2002. Extension of poroelastic analysis to double-porosity materials: New technique in microgeomechanics. *Journal of engineering mechanics*, 128(8), pp.840-847.

Biot, M. and Willis, D., 1957. The Theory of Consolidation. *J. Appl Elastic Coefficients of the Mech*, 24, pp.594-601.

Biot, M.A., 1941. General theory of three-dimensional consolidation. *Journal of applied physics*, 12(2), pp.155-164.

Bourdin, B., Chukwudozie, C.P. and Yoshioka, K., 2012, January. A variational approach to the numerical simulation of hydraulic fracturing. In *SPE Annual Technical Conference and Exhibition*. Society of Petroleum Engineers.

Chen, Z., 2013, May. An ABAQUS implementation of the XFEM for hydraulic fracture problems. In *ISRM International Conference for Effective and Sustainable Hydraulic Fracturing*. International Society for Rock Mechanics.

Chin, L.Y., Raghavan, R. and Thomas, L.K., 1998, January. Fully-coupled geomechanics and fluid-flow analysis of wells with stress-dependent permeability. In *SPE International Oil and Gas Conference and Exhibition in China*. Society of Petroleum Engineers.

Crouch, S.L., 1976. Solution of plane elasticity problems by the displacement discontinuity method. I. Infinite body solution. *International Journal for Numerical Methods in Engineering*, 10(2), pp.301-343.

Dolbow, J.E., 1999. *An extended finite element method with discontinuous enrichment for applied mechanics*. Northwestern university.

Fries, T.P. and Belytschko, T., 2010. The extended/generalized finite element method: an overview of the method and its applications. *International Journal for Numerical Methods in Engineering*, 84(3), pp.253-304.

GUO, J.C., LU, C., ZHAO, J.Z. and WANG, W.Y., 2008. Experimental research on proppant embedment [J]. *Journal of China Coal Society*, 6, p.017.

Gai, X., Dean, R.H., Wheeler, M.F. and Liu, R., 2003, January. Coupled geomechanical and reservoir modeling on parallel computers. In *SPE Reservoir Simulation Symposium*. Society of Petroleum Engineers.

Ganis, B., Mear, M.E., Sakhaee-Pour, A., Wheeler, M.F. and Wick, T., 2014. Modeling fluid injection in fractures with a reservoir simulator coupled to a boundary element method. *Computational Geosciences*, 18(5), pp.613-624.

Garipov, T.T., Karimi-Fard, M. and Tchelepi, H.A., 2014, August. Fully Coupled flow and Geomechanics Model for Fractured Porous Media. In 48th US Rock Mechanics/Geomechanics Symposium. American Rock Mechanics Association.

Gutierrez, M., Lewis, R.W. and Masters, I., 2001. Petroleum reservoir simulation coupling fluid flow and geomechanics. *SPE Reservoir Evaluation & Engineering*, 4(03), pp.164-172.

Huang, J. and Ghassemi, A., 2012, January. Geomechanical evolution of fractured reservoirs during gas production. In 46th US Rock Mechanics/Geomechanics Symposium. American Rock Mechanics Association.

Huang, R., Sukumar, N. and Prévost, J.H., 2003. Modeling quasi-static crack growth with the extended finite element method Part II: Numerical applications. *International Journal of Solids and Structures*, 40(26), pp.7539-7552.

Huitt, J.L., McGlothlin, B.B. and McDonald, J.F., 1959, January. The propping of fractures in formations in which propping sand crushes. In *Drilling and Production Practice*. American Petroleum Institute.

Huitt, J.L. and McGlothlin Jr, B.B., 1958, January. The propping of fractures in formations susceptible to propping-sand embedment. In *Drilling and Production Practice*. American Petroleum Institute.

Hajibeygi, H., Karvounis, D., Jenny, P., A hierarchical Fracture Model for the Iterative Multiscale Finite Volume Method, *Journal of Computational Physics*, 2011.

Izadi, G., Wang, S., Elsworth, D., Liu, J., Wu, Y. and Pone, D., 2011. Permeability evolution of fluid-infiltrated coal containing discrete fractures. *International Journal of Coal Geology*, 85(2), pp.202-211.

Janssen, M., Zuidema, J. and Wanhill, R.J.H., 2006. Fracture mechanics VSSD.

Jha, B. and Juanes, R., 2007. A locally conservative finite element framework for the simulation of coupled flow and reservoir geomechanics. *Acta Geotechnica*, 2(3), pp.139-153.

Jiang, J. and Younis, R.M., 2015. Numerical study of complex fracture geometries for unconventional gas reservoirs using a discrete fracture-matrix model. *Journal of Natural Gas Science and Engineering*, 26, pp.1174-1186.

Karimi-Fard, M., Durlofsky, L.J. and Aziz, K., 2003, January. An efficient discrete fracture model applicable for general purpose reservoir simulators. In *SPE Reservoir Simulation Symposium*. Society of Petroleum Engineers.

Khoei, A.R., 2014. Extended finite element method: theory and applications. John Wiley & Sons.

Kim, J., Sonnenthal, E.L. and Rutqvist, J., 2012. Formulation and sequential numerical algorithms of coupled fluid/heat flow and geomechanics for multiple porosity materials. *International Journal for Numerical Methods in Engineering*, 92(5), pp.425-456.

Kim, J., Sonnenthal, E. and Rutqvist, J., 2015. A sequential implicit algorithm of chemo-thermo-poro-mechanics for fractured geothermal reservoirs. *Computers & Geosciences*, 76, pp.59-71.

Karimi-fard, M., Firoozabadi, A., Numerical Simulation of Water Injection in Fractured Media Using the Discrete-Fracture Model and the Galerkin Method, *SPE Journal*, 2003.

Kazemi, H., Merrill, L.S., Porterfield, K.L., Zeman, P.R., Numerical Simulation of Water-Oil Flow in Naturally Fractured Reservoirs, *SPEJ*, December 1976.

Lamb, A.R., Gorman, G., Gosselin, O.R. and Onaisi, A., 2010, January. Coupled deformation and fluid flow in fractured porous media using dual permeability and explicitly defined fracture geometry. In SPE EUROPEC/EAGE Annual Conference and Exhibition. Society of Petroleum Engineers.

Lacy, L.L., Rickards, A.R. and Bilden, D.M., 1998. Fracture width and embedment testing in soft reservoir sandstone. *SPE drilling & completion*, 13(01), pp.25-29.

Levonyan, K., 2011. *Simulation of Coupled Single-phase Flow and Geomechanics in Fractured Porous Media* (Doctoral dissertation, Stanford University).

Liu, J., Chen, Z., Elsworth, D., Miao, X. and Mao, X., 2010. Evaluation of stress-controlled coal swelling processes. *International journal of coal geology*, 83(4), pp.446-455.

Li, K., Gao, Y., Lyu, Y. and Wang, M., 2015. New Mathematical Models for Calculating Proppant Embedment and Fracture Conductivity. *SPE Journal*, 20(03), pp.496-507.

Lee, S.H., Lough, M.F., Jensen, C.L., Hierarchical Modeling of Flow in Naturally Fractured Formations with Multiple Length Scales, *Water Resources Research*, 2001.

Li, L., Lee, S.H., Efficient Field-Scale Simulation of Black Oil in a Naturally Fractured Reservoir Through Discrete Fracture Networks and Homogenized Media, *SPEREE*, 2008.

Mindlin, R.D. and Deresiewicz, H., 2013. Elastic spheres in contact under varying oblique forces. *Journal of applied mechanics*, 20.

McClure, M., Babazadeh, M., Shiozawa, S. and Huang, J., 2015, February. Fully coupled hydromechanical simulation of hydraulic fracturing in three-dimensional discrete fracture networks. In *SPE Hydraulic Fracturing Technology Conference*. Society of Petroleum Engineers.

McClure, M.W. and Horne, R.N., 2010, February. Discrete fracture modeling of hydraulic stimulation in enhanced geothermal systems. In *Proceedings of the 35th Workshop on Geothermal Reservoir Engineering*.

Melenk, J.M. and Babuška, I., 1996. The partition of unity finite element method: basic theory and applications. *Computer methods in applied mechanics and engineering*, 139(1), pp.289-314.

Moës, N., Dolbow, J. and Belytschko, T., 1999. A finite element method for crack growth without remeshing. *International Journal for Numerical Methods in Engineering*, 46(1), pp.131-150.

Mohammadi, S., 2008. Extended finite element method: for fracture analysis of structures. John Wiley & Sons.

Moinfar, A., Sepehrnoori, K., Johns, R.T. and Varavei, A., 2013, February. Coupled geomechanics and flow simulation for an embedded discrete fracture model. In *SPE Reservoir Simulation Symposium*. Society of Petroleum Engineers.

Moinfar, A., Varavei, A., Sepehrnoori, K., Johns, R.T., Development of a Coupled Dual Continuum and Discrete Fracture Model for the Simulation of Unconventional Reservoirs, SPE 163647, SPE Reservoir Simulation Symposium, The Woodlands, TX, February 2013.

Monteagudo, J., Rodriguez, A. and Florez, H., 2011. Simulation of flow in discrete deformable fractured porous media. In *SPE Reservoir Simulation Symposium, SPE 141267, The Woodlands, USA*.

Singh, G., Pencheva, G., Kumar, K., Wick, T., Ganis, B. and Wheeler, M.F., 2014, February. Impact of accurate fractured reservoir flow modeling on recovery predictions. In *SPE Hydraulic Fracturing Technology Conference*. Society of Petroleum Engineers.

Terzaghi, K., 1960. From theory to practice in soil mechanics: selections from the writings of K. Terzaghi.

Thomas, L.K., Chin, L.Y., Pierson, R.G. and Sylte, J.E., 2002, January. Coupled geomechanics and reservoir simulation. In *SPE Annual Technical Conference and Exhibition*. Society of Petroleum Engineers.

Tran, D., Settari, A. and Nghiem, L., 2002, January. New iterative coupling between a reservoir simulator and a geomechanics module. In *SPE/ISRM Rock Mechanics Conference*. Society of Petroleum Engineers.

Wei, Z. and Zhang, D., 2010. Coupled fluid-flow and geomechanics for triple-porosity/dual-permeability modeling of coalbed methane recovery. *International Journal of Rock Mechanics and Mining Sciences*, 47(8), pp.1242-1253.

Wick, T., Singh, G. and Wheeler, M.F., 2015. Fluid-Filled Fracture Propagation With a Phase-Field Approach and Coupling to a Reservoir Simulator. *SPE Journal*.

Wilson, R.K. and Aifantis, E.C., 1982. On the theory of consolidation with double porosity. *International Journal of Engineering Science*, 20(9), pp.1009-1035.

Wu, K. and Olson, J.E., 2015. Simultaneous multifracture treatments: fully coupled fluid flow and fracture mechanics for horizontal wells. *SPE Journal*, 20(02), pp.337-346.

Warren, J.E. and Root, P.J., 1963. The behavior of naturally fractured reservoirs. *Society of Petroleum Engineers Journal*, 3(03), pp.245-255.

Volk, L.J., Raible, C.J., Carroll, H.B. and Spears, J.S., 1981, January. Embedment of high strength proppant into low-permeability reservoir rock. In *SPE/DOE Low Permeability Gas Reservoirs Symposium*. Society of Petroleum Engineers.